Inducible and reversible phenotypes in a novel mouse model of Friedreich's Ataxia

Vijayendran Chandran[1, #], Kun Gao[1], Vivek Swarup[1], Revital Versano[1], Hongmei Dong[1], Maria C. Jordan[3] & Daniel H. Geschwind[1,2]

[1]Program in Neurogenetics, Department of Neurology, [2]Department of Human Genetics, [3]Department of Physiology, David Geffen School of Medicine, University of California, Los Angeles, CA 90095, USA.
[#]Present address: Department of Pediatrics, School of Medicine, University of Florida, Gainesville, FL 32610-0296, USA.
Correspondence should be addressed to D.G. (dhg@mednet.ucla.edu) or V.C. (vijayendran@ufl.edu).

ABSTRACT

Friedreich's ataxia (FRDA), the most common inherited ataxia, is caused by recessive mutations that reduce the levels of frataxin (FXN), a mitochondrial iron binding protein. We developed an inducible mouse model of *Fxn* deficiency that enabled us to control the onset and progression of disease phenotypes by the modulation of *Fxn* levels. Systemic knockdown of *Fxn* in adult mice led to multiple phenotypes paralleling those observed in human patients across multiple organ systems. By reversing knockdown after clinical features appear, we were able to determine to what extent observed phenotypes represent reversible cellular dysfunction. Remarkably, upon restoration of near wild-type FXN levels, we observed significant recovery of function, associated pathology and transcriptomic dysregulation even after substantial motor dysfunction and pathology were observed. This model will be of broad utility in therapeutic development and in refining our understanding of the relative contribution of reversible cellular dysfunction at different stages in disease.

INTRODUCTION

A guanine-adenine-adenine (GAA) trinucleotide repeat expansion within the first intron of the frataxin (*Fxn*) gene in the chromosome 9 is the major cause of Friedreich's ataxia (FRDA), the most commonly inherited ataxia(1, 2). Due to recessive inheritance of this GAA repeat expansion, patients have a marked deficiency of *Fxn* mRNA and protein levels caused by reduced *Fxn* gene transcription(2, 3). Indeed, the GAA expansion size has been shown to correlate with residual *Fxn* levels, earlier onset and increased severity of disease(4, 5). The prevalence of heterozygous carriers of the GAA expansion is between 1:60 and 1:110 in European populations, and the heterozygous carriers of a *Fxn* mutation are not clinically affected(6, 7).

FRDA is an early-onset neurodegenerative disease that progressively impairs motor function, leading to ataxic gait, cardiac abnormalities, and other medical co-morbidities, ultimately resulting in early mortality (median age of death, 35 years)(8, 9). However, identification of the causal gene led to identification of a significant number of patients with late onset, they tend to have slower progression with less severe phenotype and are associated with smaller GAA expansions(10). This shorter expansion enables residual *Fxn* expression(11), thus modifying the classical FDRA phenotype, consistent with other data indicating that *Fxn* deficiency is directly related to the FRDA phenotype(12). Extra-neurologic symptoms including metabolic dysfunction and insulin intolerance are observed in the majority and frank type I diabetes is observed in approximately 15% of patients, the severity of which is related to increasing repeat length(13-15). The mechanisms by which *Fxn* reduction leads to clinical symptoms and signs remain to be elucidated, but molecular and cellular dysfunction mediated by a critical reduction in *Fxn* levels plays a central role(16).

FXN is a nuclear-encoded mitochondrial protein involved in the biogenesis of iron-sulphur clusters, which are important for the function of the mitochondrial respiratory chain activity(17, 18). Studies in mouse have shown that *Fxn* plays an important role during embryonic development, as homozygous frataxin knockout mice display embryonic lethality(19), consistent with FXN's evolutionary

48 conservation from yeast to human(2, 3). Over the past several years, multiple mouse models of
49 frataxin deficiency, including a knock-in knockout model(20), repeat expansion knock-in model(20),
50 transgenic mice containing the entire *Fxn* gene within a human yeast artificial chromosome, YG8R and
51 YG22R(21, 22), as well as a conditional *Fxn* knockout mouse, including the cardiac-specific(23) and a
52 neuron specific model(23) have been generated. These existing transgenic and heterozygous knockout
53 FRDA animal models are either mildly symptomatic, or restricted in their ability to recapitulate the
54 spatial and temporal aspects of systemic FRDA pathology when they are engineered as tissue-specific
55 conditional knockouts(20-25). Despite advances made towards elucidating FRDA pathogenesis, many
56 questions remain due to the need for mouse models better recapitulating key disease features to
57 understand frataxin protein function, disease pathogenesis and to test therapeutic agents.

58 In this regard, one crucial question facing therapeutic development and clinical trials in FRDA is
59 the reversibility of symptoms. The natural history of the disorder has been well described(26, 27), it is
60 not known how clinical features such as significant motor disability relate to reversible processes (e.g.
61 underlying neuronal dysfunction) or reflect irreversible cell death. It is often assumed that clinically
62 significant ataxia and motor dysfunction reflects neurodegeneration, although this may not be the case.
63 This issue, while critically important for therapeutic development, is difficult to address in patients, but
64 we reasoned that we could begin to address this question in an appropriate mouse model.

65 Here we report an inducible mouse model for FRDA, the FRDAkd mouse, that permits
66 reversible, and yet substantial frataxin knockdown, allowing detailed studies of the temporal
67 progression, or recovery following restoration of frataxin expression - the latter permitting exploration of
68 disease reversal given optimal treatment (normalization of *Fxn* levels). We observe that *Fxn* knockdown
69 leads to behavioral, physiological, pathological and molecular deficits in FRDAkd mice paralleling those
70 observed in patients, including severe ataxia, cardiac conduction defects and increased left ventricular
71 wall thickness, iron deposition, mitochondrial abnormalities, low aconitase activity, and degeneration of
72 dorsal root ganglia, retina, as well as early mortality. We identify a signature of molecular pathway

73 dysfunction via genome-wide transcriptome analyses, and show reversal of this molecular phenotype
74 and as well as behavioral and pathological measures, even in the setting of significant disability due to
75 motor dysfunction in FRDAkd animals.

RESULTS

RNA interference based in vivo frataxin knockdown and rescue

To investigate the neurological and cardiac effects linked to reduced FXN levels and to create a model for testing new therapies *in vivo*, we sought to generate mice that develop titratable clinical and pathological features of FRDA. We employed recombinase-mediated cassette exchange for genomic integration of a single copy shRNA transgene (doxycycline-inducible) that can mediate frataxin silencing temporally under the control of the H1 promoter via its insertion in a defined genomic locus that is widely expressed (rosa26 genomic locus)(28). This allowed us to circumvent the lethal effect of organism-wide knockout, while permitting significant frataxin reduction in all tissues. Depending on the dose of the inductor doxycycline (dox), temporal *Fxn* knockdown was achieved to control the onset and progression of the disease (**Fig. 1a**).

Six different shRNA sequences were screened in vitro to obtain a highly efficient shRNA targeting the mature coding sequence of frataxin (**Fig. 1b** and **Supplementary Fig. 1**). Transgenic animals (FRDAkd) containing a single copy of this efficient shRNA transgene (**Fig. 1b)** were generated and characterized. First, to test *Fxn* knockdown efficiency, we explored the response to dox at varying escalating doses in drinking water. At the higher doses, we observed mortality as early as two weeks and a 100% mortality rate by 5 to 6 weeks, not permitting extended time series analyses (Online Methods). We found that the combination of 2 mg/ml in drinking water coupled with 5 or 10 mg/kg intraperitoneal injection of dox twice per week, led to efficient *Fxn* knockdown within two weeks post treatment initiation, while avoiding a high early mortality rate (Online Methods). Hence, for all subsequent experiments we utilized this regimen to model the chronicity of this disorder in patients by balancing the gradual appearance of clinical signs and decline in function, while limiting early demise (**Fig. 1c**).

To determine the effect of *Fxn* deficiency in adult mice after a period of normal development (similar to a later onset phenotype in humans), which would allow establishment of stable baselines,

101 and to obtain relatively homogeneous data from behavioral tests(29) we initiated dox at 3 months.
102 Following twenty weeks with (Tg +) or without (Tg -) doxycycline administration (**Fig. 1c;** Online
103 Methods), we observed highly efficient silencing of *Fxn*, reaching greater than 90% knockdown across
104 multiple CNS and non-CNS tissues ($P < 0.05$, two-way ANOVA; **Fig. 1d,e**). Using this regimen, time
105 series western blot analyses of 80 independent animals (wildtype with dox (Wt +) N= 24; transgenic
106 with dox (Tg +) N= 24; transgenic without dox (Tg -) N= 24; transgenic with dox removal (Rescue Tg ±)
107 N= 8, at weeks 0, 3, 8, 12, 16 and 20) confirmed efficient silencing as early as 3 weeks, and efficient
108 rescue, as evidenced by normal frataxin levels, post 8 weeks dox removal ($P < 0.05$, two-way ANOVA;
109 **Fig. 1f,g**). Together, the results indicate that FRDAkd mice treated with dox are effectively FXN
110 depleted in a temporal fashion and that *Fxn* expression can be reversed efficiently by dox removal,
111 making it suitable for studying pathological and clinical phenotypes associated with FRDA.
112
113 **Frataxin knockdown mice exhibit neurological deficits**
114 The major neurologic symptom in FRDA is ataxia, which in conjunction with other neurological deficits
115 including axonal neuropathy and dorsal root ganglion loss, contributes to the gait disorder and
116 neurological disability(8, 9). So, we first determined whether *Fxn* knockdown impacted the behavior of
117 Tg and Wt mice with (+) or without (-) dox, or with dox, followed by its removal (±; the "rescue"
118 condition), leading to a total of five groups subjected to a battery of motor behavioral tasks (each group
119 N = 15-30; total mice = 108; Online Methods) (**Fig. 2a-g)**. Wt - and Wt + control groups were included
120 to access baseline and to have a control for any potential dox effect on behavior; Tg - and Tg +
121 transgenic groups were compared to examine the effect of genotype and *Fxn* knockdown on behavior;
122 The Tg ± group was included to study the effect of FXN restoration after knockdown (rescue). We
123 observed significant weight loss and reduced survival ratio (<90%) at 25 weeks with dox treatment in
124 *Fxn* knockdown animals (Tg +) when compared to other control groups ($P < 0.05$, two-way ANOVA;
125 **Fig. 2a,b**). Tg + mice exhibited a shorter distance travelled at both 12 and 24 weeks in comparison to

126 control animals, consistent with decreased locomotor activity ($P < 0.05$, two-way ANOVA; **Fig. 2c**).
127 Next, we assessed gait ataxia(9) using paw print analysis(30) (Online Methods). The *Fxn* knockdown
128 mice (Tg +) displayed reduced hind and front limb stride length when compared with Tg-, as well as the
129 Wt control + and - dox at 12 and 24 weeks, suggesting ataxic gait ($P < 0.05$, two-way ANOVA; **Fig.**
130 **2d,e** and **Supplementary Fig. 2**). Grip strength testing also showed that Tg + animals displayed defect
131 in their forelimb muscular strength at 12 and 24 weeks when compared with other groups ($P < 0.05$,
132 two-way ANOVA; **Fig. 2f**). Finally, motor coordination and balance were evaluated using the Rotarod
133 test. Whereas no significant difference in time spent on the rod before falling off was seen between Wt
134 + or Wt - or Tg - and Tg ± mice after 12 weeks post dox removal (rescue), chronically treated mice (Tg
135 + mice) from 12 weeks onward fell significantly faster, indicative of motor impairments ($P < 0.05$, two-
136 way ANOVA; **Fig. 2g**). These observations suggest that the knockdown of *Fxn* in mice causes motor
137 deficits indicative of ataxia similar to FRDA patients(9), and demonstrates the necessity of normal
138 levels of *Fxn* expression in adults for proper neurological function.
139
140 **Frataxin knockdown leads to cardiomyopathy**
141 Cardiac dysfunction is the most common cause of mortality in FRDA(31, 32). To examine impaired
142 cardiac function in FRDAkd knockdown animals, we employed electrocardiogram (ECG) and
143 echocardiogram analyses to measure electrical activity and monitor cardiac dimensions. The ECG of
144 Tg + mice displayed a significant increase in QT interval duration when compared to the other
145 control/comparison groups at both 12 and 24 weeks post dox treatment, suggesting abnormal heart
146 rate and rhythm (arrhythmia)(33) (Online Methods; $P < 0.05$, two-way ANOVA; **Fig. 3a,e**). However,
147 rescue animals (Tg ±) 12 weeks after dox removal showed normal electrocardiogram, demonstrating
148 that by restoring the FXN levels, the prolonged QT interval can be reversed ($P < 0.05$, two-way
149 ANOVA; **Fig. 3b,e**). We also observed that the Tg + animals at week 24 displayed absence of P-waves

150 suggesting an atrial conduction abnormality(34) (**Fig. 3c**), not observed in the rescued animals. Similar
151 abnormalities have been variably observed in many FRDA patients(35).
152 Progressive hypertrophic cardiomyopathy (thickening of ventricular walls) related to the severity
153 of frataxin deficiency(35-37) is frequently observed in FRDA patients(31). To confirm structural cardiac
154 abnormalities, echocardiogram analyses were performed, focusing on left ventricular function. At 12
155 weeks there was a non-significant trend towards increasing ventricular wall thickness. However, by 24
156 weeks, dox treated transgenic animals (Tg +) exhibited ventricular and posterior wall thickening,
157 suggesting hypertrophic cardiomyopathy in these animals when compared to other control groups ($P <$
158 0.05, two-way ANOVA; **Fig. 3d,f,g**). Together, these observations indicate that the transgenic mice
159 exhibit progressive cardiomyopathy due to reduced level of *Fxn*, supporting the utilization of Tg + mice
160 for examining the molecular mechanisms downstream of *Fxn* deficiency responsible for cardiac defects.
161
162 **Cardiac pathology observed with frataxin knockdown**
163 We next explored pathological consequences of FRDA knockdown in FRDAkd mice. In FRDA patients,
164 reduced frataxin induces severe myocardial remodeling, including cardiomyocyte iron accumulation,
165 myocardial fibrosis and myofiber disarray(9). Indeed, we observed substantially increased myocardial
166 iron in Tg + mice, as evidenced by increased ferric iron staining (**Fig. 4a** and **Supplementary Fig. 3**)
167 and the increased expression of iron metabolic proteins, ferritin and ferroportin at 20 weeks (**Fig. 4b**
168 and **Supplementary Fig. 3**). Cardiac fibrosis is commonly found in association with cardiac
169 hypertrophy and failure(38). Histological analysis by Masson's trichrome staining revealed excessive
170 collagen deposition in Tg + mice hearts at 20 weeks when compared to other control groups,
171 suggesting cardiac fibrosis (**Fig. 4c**). Further examination of cardiomyocyte ultrastructure by electron
172 microscopy in control mouse (Wt +) heart demonstrates normally shaped mitochondria tightly packed
173 between rows of sarcomeres (**Fig. 4d**). In contrast, Tg + mice demonstrate severe disorganization,
174 displaying disordered and irregular sarcomeres with enlarged mitochondria at 20 weeks (**Fig. 4d**). In a

175 minority of cases, but never in controls, we observed mitochondria with disorganized cristae and
176 vacuoles in Tg + mouse heart at 20 weeks, suggesting mitochondrial degeneration (**Fig. 4e**). Next, by
177 examining aconitase which is a Fe-S containing enzyme whose activity is reduced in FRDA patients(39,
178 40), activities in Tg + and other control groups, we observed decreased aconitase activity in the Tg +
179 mouse heart at 20 weeks. Together these observations suggest that the knockdown of *Fxn* in mice
180 causes cardiac pathology similar to that observed in patients(32).
181
182 **Frataxin knockdown causes neuronal degeneration**
183 In FRDA patients and mice with *Fxn* conditional knockout, a cell population that is seriously affected by
184 frataxin reduction is the large sensory neurons of dorsal root ganglia (DRG), which results in their
185 degeneration(9). As in heart tissue, lack of *Fxn* also induces mitochondrial dysfunction in the DRG(40).
186 Thus, we assessed whether mitochondrial abnormalities are observed in Tg + mice DRG neurons by
187 electron microscopy (Online Methods). As anticipated, no mitochondrial abnormalities were detected in
188 DRG neurons in control groups, but a significant increase ($P < 0.05$, two-way ANOVA) in condensed
189 mitochondria were detected in DRG neurons of Tg + mice at 20 weeks (**Fig. 5a-c,e**), but not in Tg - or
190 Wt + mice. In most cases we observed lipid-like empty vacuoles associated with condensed
191 mitochondria in DRG neurons of Tg + animals, but not in other control groups, suggesting neuronal
192 degeneration, similar to what is observed in FRDA patients(9) ($P < 0.05$, two-way ANOVA; Online
193 Methods; **Fig. 5b,c**). Previous results in human post-mortem spinal cords of FRDA patients showed a
194 decrease in axon size and myelin fibers(8). By analyzing more than 2000 axons per group in the lumbar
195 spinal cord cross-section of high-resolution electron micrographs, we observed significant reduction in
196 axonal size and myelin sheath thickness in the spinal cord samples of Tg + mice when compared to
197 other control groups at 20 weeks ($P < 0.05$, two-way ANOVA; **Fig. 5f,g**). In the cerebellum, the number
198 of Purkinje cells, the cerebellar granular and molecular layers were not altered due to *Fxn* knockdown
199 at 20 weeks (**Supplementary Fig. 4**).

200 Next we explored the visual system, because in FRDA patients, various visual field defects have
201 been reported, suggesting that photoreceptors and the retinal pigment epithelium (RPE) can be
202 affected(41, 42). By electron microscopic examination of the photoreceptors in the retina, which are
203 specialized neurons capable of phototransduction, we observed disruption in Tg + mice at 20 weeks
204 (Online Methods; **Fig. 5h**). Previous work has shown that the disruption of photoreceptors is related to
205 visual impairment(43). Similarly, we also found a significant increase in degenerating RPE cells with
206 vacuoles in Tg + mice, which is involved in light absorption and maintenance of visual function (**Fig. 5i**).
207 Together, these results suggest that *Fxn* knockdown in the CNS of adult mice results in degeneration of
208 retinal neurons.
209
210 **Gene expression changes due to frataxin knockdown**
211 Given the phenotypic parallels in the cardiac and nervous system abnormalities in FRDAkd mice with
212 chronic *Fxn* reduction following treatment with dox, we next sought to explore genome wide molecular
213 mechanisms and determine which pathways were affected in the heart and nervous system, and if they
214 were reversible. We analyzed global gene expression profiles in the heart, cerebellum and DRGs from
215 Tg +, Tg -, Wt + and Tg ± mice from 0, 3, 12, 16, 20 and plus 4, 8 weeks post dox treatment (n= 192).
216 Differential expression analyses (Online Methods) identified 1959 genes differentially expressed in Tg +
217 mice heart when compared to Wt + and Tg - mice (FDR < 5%, **Fig. 6a, Supplementary Table 1**).
218 Similarly, we observed 709 and 206 genes differentially expressed in cerebellum and DRGs of Tg +
219 mice. While cross tissue overlap in expression changes was significant, the majority of changes were
220 tissue specific; only 31% and 38% of genes that were differentially expressed in the Tg + mice
221 cerebellum and DRGs were also dysregulated in heart. Likewise, we observed a 19% overlap between
222 DRGs and cerebellum, consistent with previous observations that *Fxn* reduction causes distinct
223 molecular changes in different tissues(15).

224 Next, we analyzed these differently expressed transcripts in cardiac tissue from Tg + mice with
225 respect to cellular pathways. The top GO categories and KEGG pathways include chemotaxis, immune
226 response, lysosome and phagocytosis, vesicle transport and endocytosis, p53 signaling pathway, cell
227 cycle and division, protein transport and localization, nucleoside and nucleotide binding, and
228 mitochondrion (Benjamini corrected P-value < 0.05) (**Fig. 6a, Supplementary Table 2**). To
229 characterize the temporal patterns of these signaling cascades after frataxin knockdown and rescue,
230 we examined their time course by PCA analyses of the gene expression profiles (**Fig. 6b**). By
231 examining the cumulative explained variability of the first three principal components for these clusters
232 of genes, we show that each of these functional groups are activated as early as three weeks after dox
233 initiation (and remain elevated for up to 20 weeks); importantly, the aberrant expression of all of these
234 clusters observed in Tg + mice are largely reversed after eight weeks of rescue via *Fxn* re-expression
235 (**Fig. 6a,b**).
236 Another notable observation is that immune system activation is among the earliest pathways
237 regulated after *Fxn* knockdown (**Fig. 6b**). This suggests that initiation of immune responses (innate and
238 adaptive) is a direct consequence of *Fxn* knockdown. For example, 38 genes involved in the chemokine
239 signaling pathway (KEGG: mmu04062) were significantly differentially expressed due to *Fxn*
240 knockdown in Tg + mice heart (**Supplementary Fig. 5**). Cross validating these genes with previously
241 published gene expression datasets obtained from FRDA patients(44) and mouse models associated
242 with FRDA(20, 23), identified several genes involved in the chemokine signaling pathway (E.g.: CCL2,
243 3, 4, 7, CXCL1, 16, PRKCD, STAT3) consistently differentially expressed in these six independent
244 FRDA associated datasets (**Supplementary Fig. 6**). This implicates a vital role for chemokines and
245 immune response in FRDA pathology, as has been suggested for other neurodegenerative
246 diseases(45-48).
247
248 **Shared and tissue specific gene expression changes**

249 We next performed weighted gene co-expression network analysis (WGCNA)(49-51), a powerful
250 method for understanding the modular network structure of the transcriptome, to organize the frataxin
251 related transcriptional changes in an unbiased manner following knockdown and rescue. WGCNA
252 permits identification of modules of highly co-expressed genes whose grouping reflects shared
253 biological functions and key functional pathways, as well as key hub genes within the modules, and has
254 been widely applied to understanding disease related transcriptomes(52, 53). By applying WGCNA and
255 consensus network analysis(50) we identified 19 robust and reproducible co-expression modules
256 (Online Methods; **Supplementary Fig. 7 and Supplementary Table 3**) between the three tissues
257 datasets generated at 0, 3, 12, 16 and 20 weeks after *Fxn* knockdown and 4 and 8 weeks post dox
258 removal. On the basis of the module eigengene correlation with time-dependent changes after *Fxn*
259 knockdown, we first classified modules as up-regulated and down-regulated following knockdown
260 (**Supplementary Fig. 8**). Next, based on the significant module trait relationships (Wilcoxon P-value <
261 0.05), we identified 11 modules strongly associated with *Fxn* knockdown: three down-regulated
262 modules in two or more tissues after *Fxn* knockdown (yellow, lightgreen and turquoise) and three up-
263 regulated modules (blue, purple, and black) (**Supplementary Fig. 8**), three down-regulated modules in
264 heart, which were up-regulated in cerebellum (red, greenyellow and magenta) and two up-regulated
265 modules in heart which were down-regulated in cerebellum (cyan and pink). Although six of the gene
266 co-expression modules (yellow, lightgreen, turquoise, blue, purple, and black) in the heart, cerebellum
267 and DRG following *Fxn* knockdown are highly preserved across tissues, five modules (red,
268 greenyellow, magenta, cyan and pink) exhibit differential expression profiles suggesting tissue specific
269 molecular changes, consistent with previous observations of shared and organ specific changes(15)
270 (**Supplementary Fig. 8**).

271 As a first step toward functional annotation of the cross tissue modules, we applied GO and
272 KEGG pathway enrichment analyses, which showed enrichment (Benjamini-corrected p values < 0.05)
273 for several GO categories and pathways in the *Fxn* knockdown co-expression modules which included

274 several previously associated functional categories related with FRDA (**Supplementary Table 4**).
275 Three modules (yellow, lightgreen and turquoise) that were down-regulated in two or in all three tissues
276 due to *Fxn* knockdown included, nucleotide, nucleoside and ATP binding, myofibril assembly, muscle
277 tissue development, RNA processing, and several mitochondrial related categories: oxidative
278 phosphorylation, respiratory chain, NADH dehydrogenase activity, and electron transport chain. We
279 also observed that the genes present in turquoise module were enriched for several KEGG pathways,
280 namely, PPAR signaling (mmu03320; genes=14), insulin signaling (mmu04910; n=19), fatty acid
281 metabolism (mmu00071; n=10), cardiac muscle contraction (mmu04260; n=20), dilated
282 cardiomyopathy (mmu05414; n=13), and hypertrophic cardiomyopathy (mmu05410; n=14), which have
283 been previously associated with FRDA, reflecting the multi-systemic nature of FRDA. Similarly, three
284 upregulated cross tissue modules (blue, purple, and black) include, nucleotide binding, vesicle-
285 mediated transport, immune response (innate and adaptive), defense response, inflammatory
286 response, induction of apoptosis, positive regulation of cell death, cell adhesion, and skeletal system
287 development (**Supplementary Table 4**). These results demonstrate that unsupervised analyses can
288 identify groups of genes not only with shared biological functions, but also relevant to the clinical
289 phenotypes observed in FRDA.

290 Three tissue specific modules that were down-regulated in heart and up-regulated in cerebellum
291 (red, greenyellow and magenta) showed enrichment for, transcription regulator activity, neurological
292 system process, synaptic vesicle and nucleotide, nucleoside and ATP binding. Two other modules that
293 were up-regulated in heart and down-regulated in cerebellum (cyan and pink) were enriched for cell
294 cycle, cell division, mitosis and DNA replication (**Supplementary Table 4**). In summary, we observed
295 several metabolic functional categories that were differentially expressed (up and down) due to *Fxn*
296 knockdown. The modules consisting of mitochondrial and cardiac specific categories along with PPAR
297 signaling, insulin signaling, fatty acid metabolism pathways were down regulated in all tissues.
298 Likewise, the modules enriched for immune, apoptosis and cell death related categories we up-

299 regulated in all tissues due to *Fxn* knockdown. Synaptic and transcription regulator activity functional
300 categories were only up-regulated in cerebellum, whereas cell cycle, cell division, mitosis and DNA
301 replication related functional categories were down-regulated in cerebellum and up-regulated in the
302 heart. These general functional categories related to *Fxn* knockdown have been previously associated
303 with altered function in FRDA patients(44, 54), suggesting that genes within these modules would make
304 interesting candidate genes for follow up studies, because many of the genes have not been previously
305 associated with FRDA pathology and the disease mechanism.
306
307 **Gene expression candidate biomarkers associated with frataxin knockdown**
308 To identify candidate molecular targets and to better understand the molecular mechanism associated
309 with *Fxn* knockdown, we first manually combined all the GO ontology terms (see above and
310 **Supplementary Table 4**) that were enriched in the 11 modules into 26 broad functional categories
311 based on GO slim hierarchy (**Supplementary Table 5**) and screened for co-expressed genes within
312 each functional category in all three tissues ($r > 0.5$ and P-value < 0.05) over the time course. This
313 allowed us to identify critical functional sub-categories that are up or down regulated due to frataxin
314 knockdown and subsequently permitted us to detect differentially expressed candidate genes that are
315 co-expressed within each functional category (**Fig. 6d; Supplementary Fig. 9**). For example, we show
316 that immune, cell cycle and apoptosis related functional groups are up-regulated, whereas cardiac,
317 macromolecule and mitochondrial related functional groups were down-regulated (**Fig. 6d**). In the
318 immune category, we observed most prominent changes in complement activation pathway genes,
319 namely, C3, C4B, C1QB, C1QC and Serping1. Interesting, we also observed that many of these genes
320 were also up-regulated in peripheral blood mononuclear cells obtained from FRDA patients
321 (**Supplementary Fig. 10**), suggesting the potential for complement activation to act as a biomarker for
322 FRDA as previously suggested for other degenerative diseases(55). Similarly, we found several genes,
323 for example, CACNA2D1, ABCC9 and HRC involved in normal cardiac function, to be down-regulated

324 in heart tissue upon frataxin knockdown (**Fig. 6d**). CACNA2D1 is associated with Brugada syndrome,
325 also known as sudden unexpected nocturnal death syndrome, a heart condition that causes ventricular
326 arrhythmia(56). Mutations in ABCC9 gene can cause dilated cardiomyopathy(57) and a genetic variant
327 in the HRC gene has been linked to ventricular arrhythmia and sudden death in dilated
328 cardiomyopathy(58). These observations suggest that lower levels of frataxin causes dysregulation of
329 multiple genes related to arrhythmia or cardiac failure, a primary cause of death in FRDA patients.

330 There has been accumulating evidence suggesting that apoptosis may be an important mode of
331 cell death during cardiac failure(59). In agreement with this, we observed genes related to apoptosis
332 were up-regulated after *Fxn* knockdown in FRDAkd mice heart (**Fig. 6d**), which has been previously
333 associated with FRDA pathogenesis and reported in other *Fxn* deficiency models(24, 60, 61). In order
334 to validate our network findings, we tested CASP8 protein levels(62), observing an increase in cleaved
335 Caspase 8 protein levels in Tg + heart tissue compared with control mice (**Fig. 6e**). Next, we employed
336 the TUNEL assay to detect apoptotic cells that undergo extensive DNA degradation during the late
337 stages of apoptosis(63). However, we did not observe an increase in cell death in all tissues by TUNEL
338 staining (**Fig. 6f**).

339

340 **Literature data extraction for candidate genes associated with frataxin knockdown**

341 We next examined the phenotype-gene associations extracted by co-occurrence-based text-mining in
342 an attempt to link FRDA disease phenotypes with genes. For this, we screened the literature for
343 potential co-occurrence link association between the observed FRDAkd mice phenotypes and the
344 genes that are differentially expressed after *Fxn* knockdown (Online Methods). Identifying potential
345 biomarker candidates that are previously validated for certain phenotypes can provide insight into
346 disease progression, pathogenesis and extremely valuable for assessing therapeutic options(64). We
347 screened with the genes that are differentially expressed (FDR < 5%) and present in the co-expression
348 modules associated with behavioral and pathological key-terms (Eg: ataxia; **Supplementary Table 6**)

349 in the published literature. Interestingly, this analysis identified numerous genes in which mutations are
350 known to cause Mendelian forms of ataxia namely, ANO10(65, 66), CABC1(67, 68) and POLG(69, 70)
351 that were significantly down-regulated in the heart tissue and mildly down-regulated in the cerebellum
352 after *Fxn* knockdown in Tg + animals (**Fig. 6g and Supplementary Fig. 11**). We also found three other
353 genes that are differentially expressed due to *Fxn* knockdown, namely, CSTB(71), NHLRC1(72) and
354 PMM2(73) all of which are associated with other disorders when mutated causes ataxia (**Fig. 6g**).
355 These observations suggest that *Fxn* along with multiple other downstream candidates causes
356 behavioral deficits in FRDAkd mice. Similarly, for cardiac phenotypes, we identified multiple genes
357 related to cardiac fibrosis that were up-regulated in FRDAkd mice heart (**Fig. 6g**), including
358 LGALS3(74), ICAM1(75) and TIMP1(76) were up-regulated (**Fig. 6g**). Genes related to iron regulation,
359 included HFE(77), SLC40A1(77), HMOX1(78), TFRC(77) and GDF15(79) all of which are directly
360 involved in hemochromatosis and iron overload (**Fig. 6g**). We also found previously associated genes
361 related with muscle strength (E.g.: SRL, DCN), myelination (E.g.: PMP22, LGALS3, TLR2 and SIRT2)
362 and several genes related to neuronal degeneration (E.g.: GRN and APP) to be dysregulated in
363 FRDAkd mice (**Fig. 6g and Supplementary Fig. 11**), connecting this degenerative disorder with the
364 molecular signaling pathways known to be causally involved in other such disorders.

365 Perhaps the most prominent such known pathway associated with neurodegeneration, was
366 autophagy, since several autophagy-related genes (LAMP2, ATF4, TLR2, OPTN, MAPK14, SIRT2,
367 ICAM1, LGALS3, DCN, RCAN1, GRN) were present in these disease phenotype-associated sub
368 networks (**Fig. 6g**). Disruption of autophagy is also reported as altered in other *Fxn* deficiency
369 models(24, 60, 61) and is associated with various stress conditions including mitochondrial
370 dysfunction(80, 81). Autophagy is responsible for the recycling of long-lived and damaged organelles
371 by lysosomal degradation(82). To validate our network findings, we utilized LC3-II as a marker for
372 autophagy, showing autophagy activation in Tg + mice heart, but not in spinal cord tissue (**Fig. 6e, h**).
373 This suggests activation of apoptosis (**Fig. 6d, e**) and autophagy (**Fig. 6e, h**) may therefore potentiate

374 the cardiac dysfunction of Tg + mice. Next, by examining the expression levels of all these sub network
375 genes (**Fig. 6g**) in the datasets of other FRDA related mouse models and patient peripheral blood
376 mononuclear cells, we show that they are also differentially expressed in the same direction (**Fig. 6i**),
377 suggesting these sub network genes can be ideal candidates for molecular biomarkers in FRDA. In
378 summary, consistent with our behavioral, physiological and pathological findings, we show multiple
379 candidate genes related to key degeneration related phenotypes to be altered in FRDAkd mice.
380

381 **Rescue of behavioral, pathological and molecular changes due to frataxin restoration**

382 Our data show that mice carrying the dox inducible shRNA for *Fxn* develop normally until they are
383 challenged with dox, which subsequently results in substantial FXN reduction and causes multiple
384 behavioral and pathological features observed in patients with FRDA, including cardiac and nervous
385 system dysfunction (**Fig. 2-5**). *Fxn* knockdown mice displayed remarkable parallels with many of the
386 behavioral, cardiac, nervous system impairments along with physiological, pathological and molecular
387 deficits observed in patients. At a general level FRDAkd mice displayed weight loss, reduced locomotor
388 activity, reduced strength, ataxia and early mortality (**Fig. 2**). In the nervous system, FRDAkd mice
389 showed abnormal mitochondria and vacuolization in DRGs, retinal neuronal degeneration, and reduced
390 axonal size and myelin sheath thickness in the spinal cord(8, 9, 24, 25) (**Fig. 5**). With regards to cardiac
391 dysfunction, FRDAkd mice exhibited conduction defects, cardiomyopathy, evidence of iron overload,
392 fibrosis, and biochemical abnormalities that are commonly observed in patients(8, 9, 25) (**Fig. 3,4**).
393 These features correspond to a phenotype of substantial multisystem, clinical disability consistent with
394 moderate to severe disease after 3 months of frataxin deficiency and that lead to a 50% mortality rate
395 at approximately 5 months in these mice.

396 Given that optimal therapy in patients with FRDA could be considered replenishment of FXN
397 itself (e.g. via gene therapy(83) or improvement of *Fxn* transcription via small molecules(84)), we next
398 asked how much of the behavioral, physiological, pathological and molecular phenotype(s) observed at

399 this relatively severe stage of illness could be reversed following such “optimal” therapy. In this case,
400 optimal therapy is return of normal FXN levels under endogenous regulation through relief of
401 exogenous inhibition. Answering this question of reversibility is crucial for any clinical trial, whatever the
402 mechanism of action of the therapy, since we currently have limited information as to what represents
403 potentially reversible neurologic or cardiac phenotypes.

404 To address this, we compared two groups of mice, both transgenic and treated with dox for 12
405 weeks, at which time both groups show equivalent levels of substantial clinical features
406 (**Supplementary Fig. 12**). In one, Tg + the dox is continued for another 12 or more weeks, and in the
407 other Tg ± the dox is removed and the animals are followed. Restoration of FXN expression in *Fxn*
408 knockdown mice (Tg ±) that had reached a level of substantial clinical dysfunction led to significant
409 improvement in lifespan (no death until 20 weeks post dox removal) when compared to Tg + group
410 which resulted in 90% mortality rate by 25 week post dox treatment (**Fig. 2b**). Rescue animals (Tg ±)
411 also displayed rapidly improvement in: gait ataxia, body weight, muscle strength, locomotor activity, and
412 balance on rotarod test over the ensuing 12 week period, to a point where the treated animals were not
413 significantly different from controls on many tests (**Fig. 2**). Remarkably, we observed all of the six
414 FRDA associated clinical phenotypes tested showed significant improvement, suggesting that FRDA-
415 like neurological defects due to absence of the mouse *Fxn* gene can be rectified by delayed restoration
416 of *Fxn* (**Fig. 2**).

417 We next sought to determine whether the observed reversible behavioral changes in FRDAkd
418 mice are also accompanied by recovery of the physiological phenotype in FRDAkd mice heart, since,
419 changes in physiology offer attractive therapeutic targets for symptomatic and preventive treatment of
420 ataxia. Our results in Tg ± mice which received the dox for 12 weeks followed by 12 weeks dox removal
421 displayed reversal of long QT interval phenotype, when compared to Tg + mice at both 12 and 24
422 weeks post dox treatment (**Fig. 3a,b,e**). We observed the ventricular and posterior wall thickening only
423 at 24 weeks post dox treatment in Tg + animals (**Fig. 3d,f,g**), suggesting that long QT interval

424 phenotype is a prominent early manifestation of disease that occurs before left ventricular wall
425 thickness and show that correcting this aberrant physiology through activation of *Fxn* gene expression
426 is a potential route to therapy.

427 One question that intrigued us because of its striking behavioral and physiological functional
428 recovery is to what extent these changes represented pathological findings related to cell dysfunction
429 (potentially reversible) versus cell death (irreversible) recovery. Pathological and biochemical analyses
430 in Tg ± mice heart at post 8 weeks dox withdrawal revealed improved cardiac function displaying
431 reduced iron and ferritin accumulation, myocardial fibrosis, well ordered sarcomers, normal aconitase
432 activity and reduced mitochondrial degeneration (**Fig. 4**). Relevant to the pathogenesis of FRDA heart
433 and the role of iron and mitochondrial defect, it has been found that cells with these defects are
434 sensitized to cellular dysfunction(85, 86), and here we show this can be ameliorated by *Fxn* restoration.

435 In the nervous system of Tg ± mice post 8 weeks dox removal, we observed reduced vacuoles
436 and fewer condensed, degenerating mitochondria in DRG neurons along with several abnormal
437 mitochondria containing DRG neurons (**Fig. 5a,b,d,e**). However we only observed mild improvement in
438 myelin sheath thickness and cross section axonal size in the spinal cord of Tg ± mice during this time
439 period (**Fig. 5f,g**). Conversely, we observed a significant reduction in the number of vacuoles and
440 disrupted photoreceptors in the retina of Tg ± mice, indicating that *Fxn* restoration rescued
441 photoreceptor degeneration (**Fig. 5h,i**). These findings establish the principle of cellular dysfunction
442 reversibility in FRDAkd mouse model due to *Fxn* restoration and, therefore, raise the possibility that
443 some neurological and cardiac defects seen in this model and FRDA patients may not be permanent.

444 In line with remarkable recovery of several behavioral, physiological and pathological defects in
445 FRDAkd mice, we also observed that the genome-wide molecular biomarker represented by gene
446 expression analyses due to *Fxn* knockdown could be completely rescued after *Fxn* restoration (**Fig. 6**).
447 By rescuing the FXN protein levels back to the near basal level, we were able to reverse the molecular
448 changes completely. At post 8 weeks of dox removal after initial 12 weeks of dox treatment, we

449 examined the number of differentially expressed genes at false discovery rate of 5% in all tissues and
450 observed 100% recovery of gene expression levels in cerebellum and DRGs, and 99.95 % of reversed
451 gene expression levels in the heart of FRDAkd mice (**Fig. 6a,b**). These results which included several
452 pathways (**Fig. 6a,c,d**) that are significantly affected due to *Fxn* depletion and complete reversal (**Fig.**
453 **6a,b**) of these pathways due to *Fxn* restoration can serve as gene-expression signature for evaluation
454 of various therapeutic paradigm.

455 In summary, all six behavioral deficits in FRDAkd mice were reversed (**Fig. 2**), in the cardiac
456 system, the long QT interval phenotype along with various pathological mainfestations including
457 mitochondrial defects were reversed, in the nervous system, we observed improvement in DRGs and
458 photoreceptor neurons, and complete reversal of the molecular changes in all three tissues suggesting
459 near basal *Fxn* levels are sufficient to elevate behavioral symptoms in the preclinical FRDAkd model.
460 The rapidity of *Fxn* expression due to dox removal and its robust correction of various parameters, even
461 when restored after the onset of motor dysfunction, makes this FRDAkd mouse model an appealing
462 potential preclinical tool for testing various therapeutics for FRDA.
463
464

465 **DISCUSSION**

466 Here we report development and extensive characterization of a novel, reversible mouse model
467 of FRDA based on knock-down of frataxin by RNA interference(28), the FRDAkd mouse. Treated
468 transgenic mice developed abnormal mitochondria, exhibit cardiac and nervous system impairments
469 along with physiological, pathological and molecular deficits. These abnormalities likely contributed to
470 the behavioral phenotype of FRDAkd mice, parallel to what is observed in FRDA patients(8, 9).
471 Importantly, restoration of *Fxn* expression, even after the development of severe symptoms and
472 pathological defects, resulted in a drastic amelioration of the clinical phenotype, both in the cardiac and
473 nervous systems, including motor activity. Pathology was significantly improved in the heart, DRGs and
474 in the retina, but only mild improvement was observed in spinal cord, suggesting *Fxn* restoration for the
475 duration of 8 weeks is not sufficient for reversal of neuronal defects in the spinal cord after *Fxn*
476 knockdown. Interestingly, the patterns of gene expression changes due to *Fxn* knockdown in three
477 different tissues differed(15), indicating variable response to frataxin deficiency, which could partly
478 explain cell and tissue selectivity in FRDA(87). The onset and progression of the disease correlates
479 with the concentration of doxycycline, and the phenotype returns to baseline after its withdrawal. The
480 onset of transgene expression to achieve *Fxn* knockdown and robust recovery of symptoms due to
481 restoration of *Fxn* levels in a mouse model of FRDA, even when reversed after the onset of the
482 disease, makes this model an appealing potential preclinical tool for developing FRDA therapeutics.
483 This approach will also enable new insights into FRDA gene function and molecular disease
484 mechanisms.

485 Several models of FRDA have been developed and each have advantages and
486 disadvantages(25). This new FRDAkd model exhibits several unique features that provide advantages
487 for the study of FRDA pathophysiology relative to other existing models(20-25). First, induction of
488 frataxin knockdown permits circumventing potential confounding developmental effects(19) and has the
489 flexibility to enhance the disease onset and progression very rapidly by increasing the doxycycline

490 dose. Moreover, the temporal control of *Fxn* knockdown can provide further insights into the sequence
491 of tissue vulnerability during the disease progression(87). Second, reversibility of *Fxn* knockdown
492 provides a unique model to mimic the effect of an ideal therapeutic intervention. Along this line, it has
493 so far not been established to what extent FXN restoration after the onset of clinical motor symptoms is
494 successful to prevent occurrence and/or progression of FRDA. Therefore, this model will be of central
495 importance to gain better insights into disease pathogenesis and to test therapeutic agents. Third, the
496 doxycycline-dependent reduction of *Fxn* expression can be tailored to carefully determine the critical
497 threshold of *Fxn* levels necessary to induce selective cellular dysfunction in the nervous system (DRGs
498 and spinal cord) and to understand the occurrence of tissue specific dysfunction in FRDA. Thereby,
499 these experiments will help to understand the tissue specificity and generate clinically relevant tissue
500 targeted therapeutics for FRDA. Finally, the temporal control of single copy and reversible regulation of
501 shRNA expression against *Fxn* produces reproducible transgene expression from the well-
502 characterized rosa26 locus to generate the first model to exhibit and reverse several symptoms parallel
503 to FRDA patients. Here, we focused on the consequences of frataxin removal in an otherwise healthy
504 adult animal. However, we should emphasize that this FRDAkd model uniquely facilitates future studies
505 exploring prenatal or early post natal knockdown, and a wide variety of time course studies to
506 understand disease pathophysiology and to identify potential imaging, physiological, or behavioral
507 correlates of likely reversible or non-reversible disabilities in patients.

508 We show that FRDAkd animals are defective in several behaviors and exhibit weight loss,
509 reduced locomotor activity, reduced strength, ataxia and early mortality. All of these defects were
510 significantly improved following *Fxn* restoration, approaching or reaching wild-type levels. Most
511 importantly ataxia and survival are well-established and important clinical endpoints in FRDA(31),
512 readouts after *Fxn* restoration clearly improve these parameters and appear to be directly related to the
513 functional status of the FRDAkd mice. We conclude that *Fxn* deficient mice exhibit considerable
514 neurological plasticity even in a nervous system that is fully adult. Hence, utilizing these reversible

515 intermediate behavioral phenotypes as biomarkers will help us determine the disease progression and
516 test various FRDA treatment options in this model.

517 Hypertrophic cardiomyopathy is a common clinical feature in FRDA and approximately 60% of
518 patients with typical childhood onset FRDA die from cardiac failure(31). It is generally believed that
519 cardiac failure is caused by the loss of cardiomyocytes through activation of apoptosis(88). We
520 observed activation of early apoptosis pathways in heart tissue and severe cardiomyopathy
521 characterized by ventricular wall thickness(89). However, we did not observe TUNEL positive cells in
522 either heart or nervous system. This may reflect that the model is in a early phase of cell death
523 initiation, or rather that apoptotic cells are readily phagocytosed by neighbouring cells and are
524 consequently difficult to detect(90). We also observed enhanced activation of autophagy in the heart
525 tissue of FRDAkd mice, where autophagic cardiomyocytes are observed at a significantly higher
526 frequency during cardiac failure(91). These results suggest that apoptosis and autophagy together
527 might synergistically play a vital role in the development of cardiac defect in FRDA(92).

528 During *Fxn* knockdown, FRDAkd mice initially exhibited a long QT interval at 12 weeks during
529 electrocardiographic analyses followed by the absence of P-waves and increased ventricular wall
530 thickness at 24 weeks. Restoration of *Fxn* levels at 12 weeks reversed long QT interval phenotype.
531 However, it will be interesting to examine if the ventricular wall thickness can be restored by a more
532 prolonged rescue time period. Another prominent feature of *Fxn* deficiency mouse and FRDA patients
533 is iron accumulation and deficiency in activity of the iron-sulfur cluster dependent enzyme, aconitase, in
534 cardiac muscle(23, 40, 85, 86). Consistent with these observations, we observed increased iron
535 accumulation and reduced aconitase activity in the cardiac tissue of FRDAkd mice and we demonstrate
536 a marked reversal of both to a statistically significant extent, suggesting *Fxn* restoration is sufficient to
537 overcome and clear the iron accumulation and reverse aconitase activity(93). Our gene expression
538 data revealed several genes (HFE(77), SLC40A1(77), HMOX1(78), TFRC(77) and GDF15(79)) directly
539 involved in hemochromatosis and iron overload to be upregulated in our FRDAkd mice, all of which

540 were rescued to normal levels by frataxin restoration. Similarly, several downregulated genes involved
541 in normal cardiac function (CACNA2D1, ABCC9 and HRC) were rescued by *Fxn* restoration. Together,
542 these data indicate that *Fxn* restoration in symptomatic FRDAkd mice reverses the early development
543 of cardiomyopathy at the molecular, cellular and physiological levels.

544 Cellular dysfunction due to FXN deficiency is presumed to be the result of a mitochondrial
545 defect, since FXN localizes to mitochondria(93-95) and deficiencies of mitochondrial enzymes and
546 function have been observed in tissues of FRDA patients(40, 96). Here we show that FRDAkd mice
547 displayed accumulation of damaged mitochondria, and reduced aconitase as a direct consequence of
548 frataxin deficiency in heart, consistent with previous findings in conditional FRDA mouse models(23,
549 24), suggesting frataxin deficiency inhibits mitochondrial function leading to cellular atrophy(97).
550 Restoration of FXN resulted in improvement in pathological mitochondrial structure indicating that FXN
551 restoration prevents mitochondrial defects and may thereby enhance cell survival(93). Our observation
552 of mitochondrial dysfunction recovery as early as eight weeks after FXN restoration is consistent with
553 the highly dynamic nature of mitochondria(98).

554 In the nervous system, we observed higher level of condensed mitochondria in DRGs through
555 ultrastructural analyses. Condensed mitochondria are known to have lower respiratory control and ATP
556 production(99). On most occasions these condensed mitochondria in DRG neurons of FRDAkd mice
557 were associated with lipid-like bodies, consistent with the known close association of lipid bodies with
558 mitochondria observed in a variety of cell types(100). Of particular interest, it has been shown that the
559 junctions between these two organelles expand with an increased need for energy, suggesting the
560 direct flow of fatty acids from lipid bodies to the mitochondrial matrix for β-oxidation to meet the cell's
561 energy needs(101). We observed reduced condensed mitochondria and their association with lipid-like
562 bodies in rescue animals, suggesting that a substantial fraction of dysfunctioning frataxin-deficient
563 mitochondria containing neurons are still viable after the onset of disease and that their dysfunction can
564 be reversed. In the spinal cord, we observed reduction of axonal size and myelin sheath thickness in

565 FRDAkd animals, however after eight weeks of rescue period by FXN restoration, we observed limited
566 improvement, suggesting more time may be necessary for improved nervous system recovery.
567 Conversely, disruption of photoreceptor neurons and degenerating RPE cells in the retina displayed
568 robust recovery, indicating an overall morphological improvement in retinal neurons upon FXN
569 restoration to normal levels. These findings extend previous studies showing that many defects in
570 FRDA cells in vitro and cardiac function in vivo may be reversible following reintroduction of FXN(102)
571 by pharmacological interventions targeting aberrant signaling processes(103) or by reintroduction of
572 FXN by gene therapy(83).

573 Improved understanding of the mechanism by which FXN deficiency leads to the various
574 phenotypes observed in FRDA is a major goal of current research in this disorder. In this regard, gene
575 expression analyses identified several pathways altered, including, PPAR signaling pathway, insulin
576 signaling pathway, fatty acid metabolism, cell cycle, protein modification, lipid metabolism, and
577 carbohydrate biosynthesis, all of which have been previously associated with altered function in FRDA
578 patients(15, 54, 104). We also observed several immune components, namely, complement and
579 chemokine cascade genes being upregulated, may be implicated as a protective mechanism after *Fxn*
580 knockdown, and in a causal role through chronic activation of the inflammatory response(105, 106). It
581 will be interesting to validate these genes and pathways as potent candidate biomarkers for FRDA at
582 several stages during the disease progression.

583 Determining definitively whether the global expression changes observed in this study are
584 primary or secondary to *Fxn* knockdown will require further investigation by examining dense time
585 points immediately after *Fxn* knockdown and rescue, but our data clearly support the utility of induced
586 models of severe disease, whereby the consequences of gene depletion can be more cleanly
587 controlled to examine the molecular changes(28). Together with post-induction rescue, this study
588 highlights potential biomarkers and pathways of FRDA progression. For FRDA clinical trials, it will be
589 important to assess whether these expression changes are translatable to the human disease and

590 extend to other tissues that are more easily accessible than CNS or cardiac tissue. Together, these
591 observations suggest that this work also provides a functional genomics foundation for understanding
592 FRDA disease mechanism, progression and recovery.

593 In conclusion, our study provides multiple lines of evidence that *Fxn* knockdown in adult mice
594 leads to several symptoms parallel to FRDA patients. By restoring FXN levels we show reversal of
595 several symptoms even after significant motor defect, demonstrating the utility of this attractive model
596 for testing potential therapeutics, such as gene therapy(83), protein replacement therapy(102),
597 enhancement of mitochondrial function(107) and small molecules(108, 109). In fact, our findings
598 suggest that such approaches may not only enhance FXN expression and rescue downstream
599 molecular changes, but may too alleviate pathological and behavioral deficits associated with FRDA,
600 depending on the stage of the disorder.

601

602 **METHODS**

603 **In vitro frataxin knockdown.**

604 Six different shRNA sequence against the frataxin mRNA (**Supplementary Fig. 1**) were cloned into the
605 exchange vector (proprietary material obtained from TaconicArtemis GmbH) as described in detail
606 previously(28). N2A cells (ATCC) were transduced with exchange vectors containing the shRNA
607 against frataxin using Fugene 6 (Promega, Madison, WI). After 24 h, cells were replated in media
608 containing neomycin and were validated for efficient frataxin knockdown by RT-PCR and Western
609 blotting. Mouse LW-4 (129SvEv) embryonic stem cells were cultured and the rosa26 targeting vector
610 (from TaconicArtemis GmbH) were electroporated according to protocol described before(12). The
611 exchange vector containing validated and selected shRNA sequence
612 (GGATGGCGTGCTCACCATTAA) against the Fxn mRNA were electroporated to obtain positive ES
613 cells containing shRNA expression cassette integrated into the ROSA26 locus. Correctly targeted
614 embryonic stem cell clones were utilized to generate frataxin knockdown mice (see below).

615

616 **Frataxin knockdown transgenic mice generation.**

617 Transgenic mice were generated at UCLA Transgenic Core facility using proprietary materials obtained
618 from TaconicArtemis GmbH (Köln, Germany). In brief, mouse LW-4 (129SvEv) embryonic stem cells
619 with recombinase-mediated cassette exchange (RMCE) acceptor site on chromosome 6 were used for
620 targeting insertion of distinct Tet-On frataxin shRNA expression cassettes into the ROSA26 locus(28)
621 as depicted in **Fig. 1**. Correctly targeted embryonic stem cell clones were identified by Southern DNA
622 blot analysis and tested for frataxin mRNA knockdown at the embryonic stem cell stage (not shown).
623 One embryonic stem cell clone that gave acceptable mRNA knockdown were microinjected into
624 C57BL/6J blastocysts from which chimeric mice were derived. Frataxin knockdown mice were
625 backcrossed six generations into C57BL/6 mice.

626

627 **Genotyping.**

628 Mouse tail biopsies were collected and DNA was extracted in boiling buffer (25 mM sodium hydroxide,
629 0.2 mM EDTA) at 98°C for 60 min. Extracted DNA was neutralized in Tris/HCl buffer (pH5.5) and PCR
630 was performed under the following conditions with BioMix Red (Bioline). Four primers were used in the
631 reaction: 5'-CCATGGAATTCGAACGCTGACGTC-3', 5'-TATGGGCTATGAACTAATGACCC-3', to
632 amplify shRNA; 5'-GAGACTCTGGCTACTCATCC-3', 5'- CCTTCAGCAAGAGCTGGGGAC-3', as
633 genomic control. The cycling conditions for PCR amplification were: 95°C for 5 min; 95°C for 30 s, 60°C
634 for 30 s, 72°C for 1 min, (35 cycles); 72°C for 10 min. PCR products were analyzed by gel
635 electrophoresis using 1.5% agarose and visualized by Biospectrum imaging system (UVP).

636

637 **Animal and study design.**

638 Experiments were approved by the Animal Research Committee (ARC) of University of California, Los
639 Angeles and were in accordance with ARC regulation. Extensive neurological and neuropsychological
640 tests (body weight, poorly groomed fur, bald patches in the coat, absence of whiskers, wild-running,
641 excessive grooming, freezing, hunched body posture when walking, response to object [cotton-tip swab
642 test], visual cliff behavior analysis) were performed to ensure all animals included in the studies were
643 healthy. Age and sex were matched between wild type (Wt) and transgenic (Tg) groups to eliminate
644 study bias. The average age of the animals at the start of experiments was 3-4 months. Three different
645 study cohorts were implemented: behavior, pathology and gene expression. Animals were randomly
646 assigned to different experimental groups with in these three different study cohorts before the start of
647 experiments. Due to high mortality rate of FRDAkd animals, we doubled the Tg + animal number (a
648 sample size of 30 animals per Tg + treatment group for behavioral analyses (60 total)) in order to have
649 sufficient power for statistical analyses. All the group size for our experiments were determined by
650 statistical power analysis. The values utilized were: the power = 0.9, alpha = 0.05, Coefficient of

651 determination = 0.5, effect size = 0.70. Effect size and power calculations were based on our pilot
652 experiments.
653
654 **In vivo frataxin knockdown.**
655 Animals were divided into the following groups: Wt treated with doxycycline (Dox) (Wt +), Wt without
656 Dox (Wt -), Tg treated with Dox (Tg +), Tg without Dox (Tg -), Tg Dox rescue (Tg ±). First, we examined
657 the Tg + mice for frataxin knockdown utilizing higher dose of dox (4 and 6mg/ml), we observed mortality
658 as early as two weeks and a 100% mortality rate by 5 to 6 weeks (not shown). To avoid early mortality
659 and to have slow and steady state of disease progression we followed 2 mg/ml in drinking water
660 coupled with intraperitoneal injection of dox (5 or 10 mg/kg) twice per week. Doxycycline (2mg/mL) was
661 added to the drinking water of all treatment animals which was changed weekly. In addition, animals
662 were injected intraperitoneally (IP) with Dox (5 mg/kg body weight) twice a week for 10 weeks followed
663 by 10 mg Dox/kg body weight twice a week for 2 weeks. Animals in Tg Dox rescue (Tg ±) group were
664 given untreated water and not injected with Dox after week 12. All animals were weighed weekly.
665
666 **Behavior cohort.**
667 *Animal information.* A total of 108 animals (Wt n=32, Tg n=76) were included in this study with equal
668 numbers of male and female animals. For all tests, investigators were blinded to genotype and
669 treatment. For all behavioral tests, the variance between all the groups for that specific behavioral test
670 were observed to be initially not statistically significant.
671
672 *Accelerating Rotarod.* To measure motor function, rotarod analysis was performed weekly at the start of
673 Dox treatment using an accelerating rotorod (ROTOMEX-5, Columbus Instruments, Columbus, OH).
674 Mice were assessed for 36 weeks. Briefly, after habituation, a mouse was placed on the rotarod
675 rotating at 5 rpm for one min and then the rotorod was accelerated at 0.09 rpm/sec^2. The latency to fall

676 from a rotating rod after acceleration was recorded. Each mouse was subjected to 3 test trials within
677 the same day with a 15 min inter-trial interval. The average latency normalized by the mouse body
678 weight in the test week was used for data analysis.
679
680 *Grip strength test.* The grip strength was measured at week 0, 12 and 24 weeks using a digital force
681 gauge (Chatillon Force Measurement Systems, AMETEK TCI Division, Largo, FL). Briefly, the mouse
682 was allowed to grasp the steel wired grid attached to the force gauge with only forepaws. The mouse
683 was then pulled back from the gauge. The force applied to the grip immediately before release of the
684 grip is recorded as the "peak tension" and is a measurement of forepaw strength. The same
685 measurement was repeated with the mouse grasping the grid with all paws for whole grip strength.
686 Each mouse was subjected to three forepaw and whole strength measurements. The hindpaw grip
687 strength was calculated as the average whole grip strength minus average forepaw strength. The value
688 of hindpaw grip strength normalized by the mouse body weight in the test week was used for data
689 analysis.
690
691 *Gait analyses.* Gait analysis was performed at week 0, 12 and 24 weeks by allowing the animals to
692 walk through a 50-cm-long, 10-cm-wide runway that was lined with blank index cards. After a period of
693 habituation (walking through the runway three times), hind and fore paws were coated with nontoxic red
694 and purple paint respectively and the mouse was allowed to walk through the runway again. Footprints
695 were captured on the index cards. The index cards were scanned and the images were measured in
696 image J for calculating the stride length and other parameters.
697
698 *Open field analyses*. Open field testing was performed at week 0, 12 and 24 weeks. Mice were placed
699 in a clear plexiglass arena (27.5 cm by 27.5 cm) with a video monitoring system that recorded any

700 movements of the mouse within the chamber for 20 min. Locomotor activity of the mice was analyzed
701 by TopScan (CleverSys) software.
702
703 **Pathology cohort.**
704 *Animal information.* A total of 57 animals (Wt n=21 (10 females, 11 males), Tg n=36 (20 females, 16
705 males)) were euthanized in the study. Animals were deeply anesthetized with sodium pentobarbital (40
706 mg/kg body weight) and perfused intracardially with 20 mL PBS (5 mL/min) followed by 20 mL freshly
707 made 4% paraformaldehyde (5 mL/min). Tissue from liver, lung, spleen, pancreas, kidney, heart, eye
708 (retina), brain, muscle, spinal cord, dorsal root ganglion (DRG) and sciatic nerve was dissected and
709 collected immediately after perfusion. Collected tissue was immersed in 4% paraformaldehyde
710 overnight at 4°C and then transferred and kept in 40% sucrose at 4°C until embedded with O.C.T.
711 Tissue cryosections (5 μM) were collected with a cryostat for staining.
712
713 *Staining.* H & E staining was performed in Translational Pathology Core Laboratory at UCLA. The
714 method is described briefly below. After equilibration, the tissue section was stained with Harris
715 Modified Hematoxylin for 10 min, then in Eosin Y for 10 min. Gomori's iron staining and Masson's
716 trichrome staining were performed in Histopathology lab in UCLA, the procedure is described briefly as
717 below. Gomori's iron staining: the tissue section was immersed for 20 min in equal parts of 20%
718 hydrochloric acid and 10% potassium ferrocyanide, washed thoroughly in distilled water. After
719 counterstaining with Nuclear Fast Red (0.1% Kernechtrot in 5% aluminum sulfate), the slides were
720 dehydrated through gradual ethyl alcohol solutions and mounted for imagining. Masson's trichrome
721 staining: the tissue section was fixed in Bouin's fixative (75 mL picric acid saturated aqueous solution,
722 25 mL of 40% formaldehyde, 5 mL glacial acetic acid) for 60 min at 60°C, stained with Weigert iron
723 hematoxylin (0.5% hematoxylin, 47.5% alcohol, 0.58% ferric chloride, 0.5% hydrochloric acid) for 10
724 min, Biebrich scarlet-acid fuchsin (0.9% Biebrich scarlet, 0.1% acid fuchsin, 1% glacial acetic acid) for

725 10 min, immersed in phosphomolybdic-phosphotungstic solution (2.5% phosphomolybdic acid, 2.5%
726 phosphotungstic acid) for 7 min, stained with aniline blue solution (2.5% aniline blue, 2% acetic acid) for
727 7 min, dehydrate and mounted for imagining. Immunofluorescence staining was performed as followed:
728 cryosections were equilibrated with TBS (20 mM Tris pH7.5, 150 mM NaCl) and permeabilized in TBST
729 (TBS with 0.2% TritonX-100). Tissue sections were incubated with primary antibody in TBST with 4%
730 normal goat serum (Jackson Immuno Research) (4°C, overnight), followed by incubation with
731 secondary antibody in TBST with 4% normal goat serum (room temperature, 2 hrs) the next day. The
732 tissue section was mounted with ProLong Gold with DAPI (ThermoFisher Scientific) and stored in the
733 dark. The following antibodies were used: anti-ferroportin-1 (LifeSpan BioSciences, LS-B1836, rabbit,
734 1:200), anti-ferritin (Abcam, ab69090, rabbit, 1:500), anti-LC3 (Abgent, AM1800a, mouse, 1:200), anti-
735 NeuN (EMD Millipore, ABN91, chicken, 1:500), anti-NeuN (EMD Millipore, ABN78, rabbit, 1:500).
736 Secondary antibodies conjugated with Alexa Fluor (ThermoFisher Scientific, 1:500) were used as
737 indicated: Alexa Fluor 488 (goat anti-Rabbit IgG, A-11008), Alexa Fluor 594 (goat anti-chicken IgG, A-
738 11039), and Alexa Fluor 488 (goat anti-mouse IgG, A-11029). DNA strand breaks were determined by
739 TUNEL assay (Roche). Briefly, sections were equilibrated with PBS, permeabilized in 0.1% Triton X-
740 100 in 0.1% sodium citrate (on ice, 2 min) and incubated with TUNEL reaction mixture in a humidified
741 atmosphere (37°C, 60 min). Sections were mounted with ProLong Gold with DAPI and stored in the
742 dark.
743
744 *Imaging and quantification.* Slides stained for hematoxylin-eosin, iron, and trichrome were scanned (20
745 x magnification) by Aperio ScanScope with Aperio ImageScope Software (Leica). Immunofluorescence
746 staining and TUNEL staining were imaged with LSM780 confocal microscope system (Zeiss). Images
747 were quantified by CellProfiler. For Purkinje cell quantification, the H&E images were scanned,
748 visualized and exported by ImageScope (Leica Biosystems) system. Exported images were utilized to

749 count the Purkinje cells manually using NIH ImageJ software. Counters were blinded to genotype and
750 treatment.
751
752 *Electron microscopy analyses.* A total of 29 animals (Wt n=9 (4 females, 5 males), Tg n=20 (9 females,
753 11 males)) were used in the study. Mice were perfused transcardially with 2.5% glutaraldehyde, 2%
754 paraformaldehyde in 0.1M phosphate buffer, 0.9% sodium chloride (PBS). Pieces of heart, lumbar
755 spinal cord, dorsal root ganglia, muscle, and eye were dissected, postfixed for 2 hours at room
756 temperature in the same fixative and stored at 4°C until processing. Tissues were washed with PBS,
757 postfixed in 1% OsO4 in PB for 1 hour, dehydrated in a graded series of ethanol, treated with propylene
758 oxide and infiltrated with Eponate 12 (Ted Pella) overnight. Tissues were embedded in fresh Eponate,
759 and polymerized at 60°C for 48 hours. Approximately 60-70 nm thick sections were cut on a RMC
760 Powertome ultramicrotome and picked up on formvar coated copper grids. The sections were stained
761 with uranyl acetate and Reynolds lead citrate and examined on a JEOL 100CX electron microscope at
762 60kV. Images were collected on type 4489 EM film and the negatives scanned to create digital files.
763 These high quality digital images were utilized to quantify the number of condensed mitochondria.
764 Condensed mitochondria, vacuoles with condensed mitochondria, and vacuoles alone were manually
765 counted with NIH ImageJ software. Animal genotype and treatment information was blinded to the
766 person who conducted the evaluation.
767
768 **Gene expression cohort.**
769 *Sample collection.* A total of 80 animals (Wt n=24 (12 females and 12 males), Tg n=56 (31 females and
770 25 males)) were sacrificed and tissue was collected in this study. Animals were sacrificed at week 0, 3,
771 8, 12, 16, 20 and plus 4, 8 weeks post dox treatment (rescue). Mouse was sacrificed by cervical
772 dislocation and tissue from liver, lung, spleen, pancreas, kidney, heart, eye (retina), brain, muscle,
773 spinal cord, dorsal root ganglion (DRG) and sciatic nerve was dissected and rinsed in cold PBS quickly

774 (3X) to remove blood. Tissue samples were transferred immediately into 2 mL RNase-free tubes and
775 immersed into liquid nitrogen. The collected tissue was stored in -80°C freezer immediately.
776
777 *RNA extraction.* Heart, cerebellum and DRG neuron samples from week 0, 3, 12, 16, 20 and 4, 8
778 weeks post dox treatment (rescue) with four biological replicates were used for expression profiling.
779 Samples were randomized prior to RNA extraction to eliminate extraction batch effect. Total RNA was
780 extracted using the miRNeasy mini kit (Qiagen) according to manufacturer's protocol and including an
781 on-column DNase digest (RNase free DNAse set; Qiagen). RNA samples were immediately aliquoted
782 and stored at -80°C. RNA concentration and integrity were later determined using a Nanodrop
783 Spectrophotometer (ThermoFisher Scientific) and TapeStation 2200 (Agilent Technologies),
784 respectively.
785
786 *Transcriptome profiling by microarray*. One hundred nanograms of RNA from heart and cerebellum
787 tissue was amplified using the Illumina TotalPrep-96 RNA Amplification kit (ThermoFisher Scientific)
788 and profiled by Illumina mouse Ref 8 v2.0 expression array chips. For DRG samples 16.5 ng of RNA
789 was amplified using the Ovation® PicoSL WTA System V2 kit (NuGEN). Only RNA with RIN greater
790 than 7.0 was included for the study. A total of 64 RNA samples for each tissue (n= 192 arrays) were
791 included and samples were randomized before RNA amplification to eliminate microarray chip batch
792 effect. Raw data was log transformed and checked for outliers. Inter-array Pearson correlation and
793 clustering based on variance were used as quality-control measures. Quantile normalization was used
794 and contrast analysis of differential expression was performed by using the LIMMA package(32).
795 Briefly, a linear model was fitted across the dataset, contrasts of interest were extracted, and
796 differentially expressed genes for each contrast were selected using an empirical Bayes test
797 statistic(32).
798

799 *Construction of co-expression networks.* A weighted gene co-expression network was constructed for
800 each tissue dataset to identify groups of genes (modules) associated with temporal pattern of
801 expression changes due to frataxin knockdown and rescue following a previously described
802 algorithm(49, 110). Briefly, we first computed the Pearson correlation between each pair of selected
803 genes yielding a similarity (correlation) matrix. Next, the adjacency matrix was calculated by raising the
804 absolute values of the correlation matrix to a power (β) as described previously(49). The parameter β
805 was chosen by using the scale-free topology criterion(49), such that the resulting network connectivity
806 distribution best approximated scale-free topology. The adjacency matrix was then used to define a
807 measure of node dissimilarity, based on the topological overlap matrix, a biologically meaningful
808 measure of node similarity(49). Next, the probe sets were hierarchically clustered using the distance
809 measure and modules were determined by choosing a height cutoff for the resulting dendrogram by
810 using a dynamic tree-cutting algorithm(49).
811
812 *Consensus module analyses.* Consensus modules are defined as sets of highly connected nodes that
813 can be found in multiple networks generated from different datasets (tissues). Consensus modules
814 were identified using a suitable consensus dissimilarity that were used as input to a clustering
815 procedure, analogous to the procedure for identifying modules in individual sets as described
816 elsewhere(111). Utilizing consensus network analysis, we identified modules shared across different
817 tissue data sets after frataxin knockdown and calculated the first principal component of gene
818 expression in each module (module eigengene). Next, we correlated the module eigengenes with time
819 after frataxin knockdown to select modules for functional validation.
820
821 *Gene Ontology, pathway and PubMed analyses.* Gene ontology and pathway enrichment analysis was
822 performed using the DAVID platform (DAVID, https://david.ncifcrf.gov/(112)). A list of differentially
823 regulated transcripts for a given modules were utilized for enrichment analyses. All included terms

824 exhibited significant Benjamini corrected P-values for enrichment and generally contained greater than
825 five members per category. We used PubMatrix(113) to examine each differentially expressed gene's
826 association with the observed phenotypes of FRDAkd mice in the published literature by testing
827 association with the key-words: ataxia, cardiac fibrosis, early mortality, enlarged mitochondria, excess
828 iron overload, motor deficits, muscular strength, myelin sheath, neuronal degeneration, sarcomeres,
829 ventricular wall thickness, and weight loss in the PubMed database for every gene.
830
831 *Data Availability.* Datasets generated and analyzed in this study are available at Gene Expression
832 Omnibus. Accession number: GSE98790.
833
834 **Quantitative real-time PCR**.
835 RT-PCR was utilized to measure the mRNA expression levels of frataxin in order to identify and
836 validate potent shRNA sequence against frataxin gene. The procedure is briefly described below: 1.5
837 µg total RNA, together with 1.5 µL random primers (ThermoFisher Scientific, catalog# 48190-011), 1.5
838 µL 10 mM dNTP (ThermoFisher Scientific, catalog# 58875) and RNase-free water up to 19.5 µL, was
839 incubated at 65 °C for 5 min, then on ice for 2 min; 6 µL first strand buffer, 1.5 µL 0.1 M DTT, 1.5 µL
840 RNaseOUT (ThermoFisher Scientific, catalog# 100000840) and 1.5 µL SuperScript III (ThermoFisher
841 Scientific, catalog# 56575) were added to the mixture and incubated for 5 min at 25 °C, followed by 60
842 min at 50 °C, and 15 min at 70 °C. The resulted cDNA was diluted 1:10 and 3 µL was mixed with 5 µL
843 SensiFast SYBR No-ROX reagent (Bioline, catalog# BIO-98020), 0.6 µL primer set (forward and
844 reverse, 10 mM) and 1.4 µL nuclease free water for real-time PCR. Each reaction was repeated three
845 times on LightCycler 480 II (Roche, catalog# 05015243001). The thermocycling program is as
846 following: 95 °C 5min; 95 °C 10 sec, 60 °C 10 sec, 72 °C 10 sec, repeat 45 cycles; 95 °C 5 sec, 65 °C 1
847 min, 97 °C 5 min.
848

849 **Western blotting.**

850 Prior to samples being analyzed by Western blotting, protein concentration was estimated by Bradford
851 assay (Bio-Rad). Proteins were separated by SDS-PAGE and transferred onto PVDF membranes. The
852 membranes were incubated with primary and secondary antibodies for protein detection. The target
853 bands were detected with antibodies: anti-Frataxin (Santa Cruz Biotechnology, sc-25820, rabbit,
854 1:200), anti-Akt (Cell Signaling Technology, #4691, rabbit, 1:500), anti-β-Actin (Sigma, #A1978, mouse,
855 1:1000), anti-Caspase 8 (rabbit monoclonal, Cell Signaling Technology, #8592S, rabbit, 1:200), anti-
856 LC3 (Abgent, # AM1800a, mouse, 1:200) and goat-anti-rabbit or goat-anti-mouse HRP-conjugated
857 secondary antibodies (ThermoFisher Scientific, #31460, and #32230, respectively,1:5000). Image J
858 was used for band quantification.

859

860 **Enzyme activity assay.**

861 Proteins from heart tissue for all genotypes at week 20 was extracted in Tris buffer (50 mM Tris-HCl pH
862 7.4). Around 80 mg of tissue was homogenized with 100 μL Tris buffer, and centrifuged at 800 g for 10
863 min at 4°C. The supernatant was transferred to a clean tube and stored at -80°C freezer immediately
864 for later use. Protein concentration was estimated by Bradford assay. Total of 5 μg of protein was used
865 to determine aconitase activity by aconitase assay kit (Cayman Chemical, catalog# 705502). The
866 absorbance of the reaction mixture at 340 nm was measured every minute for 60 min at 37°C, by
867 Synergy-2 (BioTek) plate reader. The linear phase was used to calculate the enzyme activity. 5 μg of
868 protein was used to measure citrate synthase activity by citrate synthase assay kit (Sigma, catalog#
869 CS0720). The absorbance of the reaction mixture at 412 nm was measured by Synergy-2 plate reader
870 every 31 seconds for 30 min at room temperature. The linear phase was used to calculate the enzyme
871 activity. Aconitase activity in each sample was normalized to the citrate synthase activity from the same
872 sample for comparison.

873

874 **Echocardiography.**

875 Echocardiography was performed on all the mice with a Siemens Acuson Sequoia C256 instrument
876 (Siemens Medical Solutions, Mountain View, California). The mice were sedated with isoflurane
877 vaporized in oxygen (Summit Anesthesia Solutions, Bend Oregon). Left ventricular dimensions (EDD,
878 end diastolic dimension; ESD, end systolic dimension; PWT, posterior wall thickness; VST, ventricular
879 septal thickness) were obtained from 2D guided M-mode and was analyzed using AccessPoint
880 software (Freeland System LLC, Santa Fe, New Mexico) during systole and diastole. Left ventricular
881 mass was calculated as described previously(18). Heart rate, aortic ejection time, aortic velocity and
882 mitral inflow E & A wave amplitudes were determined from Doppler flow images. Indices of contractility
883 such as left ventricular fractional shortening (LVFS), velocity of circumferential fiber shortening (VCF)
884 and ejection fraction (EF) was obtained from the images. During the procedure, heart rates were
885 maintained at physiological levels by monitoring their electrocardiograms (ECG).

886

887 **Surface ECG.**

888 Electrocardiogram (ECG) were obtained in all the mice under Isoflurane anesthesia by inserting two Pt
889 needle electrodes (Grass Technologies, West Warwick, RI) under the skin in the lead II configuration as
890 described previously(27). The mice were studied between 10 and 30 minutes to elucidate any rhythm
891 alteration. The ECG data were amplified (Grass Technologies) and then digitized with HEM V4.2
892 software (Notocord Systems, Croissy sur Seine, France). Measurements of HR, PR, RR, QRS, QT
893 intervals were obtained for comparison and statistical analysis among all the mice groups.

894

895 **Accession codes.** Gene Expression Omnibus: Datasets generated and analyzed in this study are
896 available at GEO accession: GSE98790.

897

898 **ACKNOWLEDGMENTS**

We gratefully acknowledge support from the Friedreich's Ataxia Research Alliance to D.H.G. and V.C. (including a New Investigator Award to V.C.), and the Dr. Miriam and Sheldon G. Adelson Medical Research Foundation to D.H.G.. We thank Marianne Cilluffo for assistance with electron microscopy at the BRI Electron Microscopy Core Facility at UCLA.

AUTHOR CONTRIBUTIONS

V.C. and D.H.G. designed the experiments and wrote the manuscript. K.G., R.V., H.D., and V.C. performed the behavioral, pathological, biochemical and molecular experiments. V.C. conducted or coordinated all the experiments discussed in this manuscript with input from D.H.G.. V.S. performed network analyses and V.C. performed all subsequent bioinformatic analyses. M.J. and V.C. conducted and coordinated electrocardiogram and echocardiogram analyses. All authors discussed the results and provided comments and revisions on the manuscript.

912 **REFERENCES:**
913
914 1. Chamberlain S, Shaw J, Rowland A, Wallis J, South S, Nakamura Y, von Gabain A, Farrall M,
915 Williamson R. Mapping of mutation causing Friedreich's ataxia to human chromosome 9. Nature. 1988
916 Jul 21;334(6179):248-50. PubMed PMID: 2899844.
917 2. Campuzano V, Montermini L, Molto MD, Pianese L, Cossee M, Cavalcanti F, Monros E, Rodius
918 F, Duclos F, Monticelli A, Zara F, Canizares J, Koutnikova H, Bidichandani SI, Gellera C, Brice A,
919 Trouillas P, De Michele G, Filla A, De Frutos R, Palau F, Patel PI, Di Donato S, Mandel JL, Cocozza S,
920 Koenig M, Pandolfo M. Friedreich's ataxia: autosomal recessive disease caused by an intronic GAA
921 triplet repeat expansion. Science. 1996 Mar 8;271(5254):1423-7. PubMed PMID: 8596916.
922 3. Campuzano V, Montermini L, Lutz Y, Cova L, Hindelang C, Jiralerspong S, Trottier Y, Kish SJ,
923 Faucheux B, Trouillas P, Authier FJ, Durr A, Mandel JL, Vescovi A, Pandolfo M, Koenig M. Frataxin is
924 reduced in Friedreich ataxia patients and is associated with mitochondrial membranes. Human molecular
925 genetics. 1997 Oct;6(11):1771-80. PubMed PMID: 9302253.
926 4. Filla A, De Michele G, Cavalcanti F, Pianese L, Monticelli A, Campanella G, Cocozza S. The
927 relationship between trinucleotide (GAA) repeat length and clinical features in Friedreich ataxia.
928 American journal of human genetics. 1996 Sep;59(3):554-60. PubMed PMID: 8751856. Pubmed
929 Central PMCID: 1914893.
930 5. Montermini L, Richter A, Morgan K, Justice CM, Julien D, Castellotti B, Mercier J, Poirier J,
931 Capozzoli F, Bouchard JP, Lemieux B, Mathieu J, Vanasse M, Seni MH, Graham G, Andermann F,
932 Andermann E, Melancon SB, Keats BJ, Di Donato S, Pandolfo M. Phenotypic variability in Friedreich
933 ataxia: role of the associated GAA triplet repeat expansion. Annals of neurology. 1997 May;41(5):675-
934 82. PubMed PMID: 9153531.
935 6. Andermann E, Remillard GM, Goyer C, Blitzer L, Andermann F, Barbeau A. Genetic and family
936 studies in Friedreich's ataxia. The Canadian journal of neurological sciences Le journal canadien des
937 sciences neurologiques. 1976 Nov;3(4):287-301. PubMed PMID: 1000412.
938 7. Harding AE. Friedreich's ataxia: a clinical and genetic study of 90 families with an analysis of
939 early diagnostic criteria and intrafamilial clustering of clinical features. Brain : a journal of neurology.
940 1981 Sep;104(3):589-620. PubMed PMID: 7272714.
941 8. Koeppen AH, Mazurkiewicz JE. Friedreich ataxia: neuropathology revised. Journal of
942 neuropathology and experimental neurology. 2013 Feb;72(2):78-90. PubMed PMID: 23334592. Pubmed
943 Central PMCID: 3817014.
944 9. Koeppen AH. Friedreich's ataxia: pathology, pathogenesis, and molecular genetics. Journal of the
945 neurological sciences. 2011 Apr 15;303(1-2):1-12. PubMed PMID: 21315377. Pubmed Central PMCID:
946 3062632.
947 10. Bhidayasiri R, Perlman SL, Pulst SM, Geschwind DH. Late-onset Friedreich ataxia: phenotypic
948 analysis, magnetic resonance imaging findings, and review of the literature. Archives of neurology.
949 2005 Dec;62(12):1865-9. PubMed PMID: 16344344.
950 11. Li Y, Lu Y, Polak U, Lin K, Shen J, Farmer J, Seyer L, Bhalla AD, Rozwadowska N, Lynch DR,
951 Butler JS, Napierala M. Expanded GAA repeats impede transcription elongation through the FXN gene
952 and induce transcriptional silencing that is restricted to the FXN locus. Human molecular genetics. 2015
953 Dec 15;24(24):6932-43. PubMed PMID: 26401053. Pubmed Central PMCID: 4654050.
954 12. Seibler J, Kuter-Luks B, Kern H, Streu S, Plum L, Mauer J, Kuhn R, Bruning JC, Schwenk F.
955 Single copy shRNA configuration for ubiquitous gene knockdown in mice. Nucleic acids research. 2005
956 Apr 14;33(7):e67. PubMed PMID: 15831785. Pubmed Central PMCID: 1079974.

957 13. Martinez AR, Moro A, Abrahao A, Faber I, Borges CR, Rezende TJ, Martins CR, Jr., Moscovich
958 M, Munhoz RP, Segal SL, Arruda WO, Saraiva-Pereira ML, Karuta S, Pedroso JL, D'Abreu A, Jardim
959 LB, Lopes-Cendes I, Barsottini OG, Teive HA, Franca MC, Jr. Nonneurological Involvement in Late-
960 Onset Friedreich Ataxia (LOFA): Exploring the Phenotypes. Cerebellum. 2016 Jan 11. PubMed PMID:
961 26754264.
962 14. Galea CA, Huq A, Lockhart PJ, Tai G, Corben LA, Yiu EM, Gurrin LC, Lynch DR, Gelbard S,
963 Durr A, Pousset F, Parkinson M, Labrum R, Giunti P, Perlman SL, Delatycki MB, Evans-Galea MV.
964 Compound heterozygous FXN mutations and clinical outcome in friedreich ataxia. Annals of neurology.
965 2016 Mar;79(3):485-95. PubMed PMID: 26704351.
966 15. Coppola G, Marmolino D, Lu D, Wang Q, Cnop M, Rai M, Acquaviva F, Cocozza S, Pandolfo
967 M, Geschwind DH. Functional genomic analysis of frataxin deficiency reveals tissue-specific alterations
968 and identifies the PPARgamma pathway as a therapeutic target in Friedreich's ataxia. Human molecular
969 genetics. 2009 Jul 01;18(13):2452-61. PubMed PMID: 19376812. Pubmed Central PMCID: 2694693.
970 16. Pandolfo M. The molecular basis of Friedreich ataxia. Advances in experimental medicine and
971 biology. 2002;516:99-118. PubMed PMID: 12611437.
972 17. Abrahao A, Pedroso JL, Braga-Neto P, Bor-Seng-Shu E, de Carvalho Aguiar P, Barsottini OG.
973 Milestones in Friedreich ataxia: more than a century and still learning. Neurogenetics. 2015
974 Jul;16(3):151-60. PubMed PMID: 25662948.
975 18. Tanaka N, Dalton N, Mao L, Rockman HA, Peterson KL, Gottshall KR, Hunter JJ, Chien KR,
976 Ross J, Jr. Transthoracic echocardiography in models of cardiac disease in the mouse. Circulation. 1996
977 Sep 01;94(5):1109-17. PubMed PMID: 8790053.
978 19. Cossee M, Puccio H, Gansmuller A, Koutnikova H, Dierich A, LeMeur M, Fischbeck K, Dolle
979 P, Koenig M. Inactivation of the Friedreich ataxia mouse gene leads to early embryonic lethality without
980 iron accumulation. Human molecular genetics. 2000 May 1;9(8):1219-26. PubMed PMID: 10767347.
981 20. Miranda CJ, Santos MM, Ohshima K, Smith J, Li L, Bunting M, Cossee M, Koenig M,
982 Sequeiros J, Kaplan J, Pandolfo M. Frataxin knockin mouse. FEBS letters. 2002 Feb 13;512(1-3):291-7.
983 PubMed PMID: 11852098.
984 21. Al-Mahdawi S, Pinto RM, Ruddle P, Carroll C, Webster Z, Pook M. GAA repeat instability in
985 Friedreich ataxia YAC transgenic mice. Genomics. 2004 Aug;84(2):301-10. PubMed PMID: 15233994.
986 22. Al-Mahdawi S, Pinto RM, Varshney D, Lawrence L, Lowrie MB, Hughes S, Webster Z, Blake J,
987 Cooper JM, King R, Pook MA. GAA repeat expansion mutation mouse models of Friedreich ataxia
988 exhibit oxidative stress leading to progressive neuronal and cardiac pathology. Genomics. 2006
989 Nov;88(5):580-90. PubMed PMID: 16919418. Pubmed Central PMCID: 2842930.
990 23. Puccio H, Simon D, Cossee M, Criqui-Filipe P, Tiziano F, Melki J, Hindelang C, Matyas R,
991 Rustin P, Koenig M. Mouse models for Friedreich ataxia exhibit cardiomyopathy, sensory nerve defect
992 and Fe-S enzyme deficiency followed by intramitochondrial iron deposits. Nature genetics. 2001
993 Feb;27(2):181-6. PubMed PMID: 11175786.
994 24. Simon D, Seznec H, Gansmuller A, Carelle N, Weber P, Metzger D, Rustin P, Koenig M, Puccio
995 H. Friedreich ataxia mouse models with progressive cerebellar and sensory ataxia reveal autophagic
996 neurodegeneration in dorsal root ganglia. The Journal of neuroscience : the official journal of the
997 Society for Neuroscience. 2004 Feb 25;24(8):1987-95. PubMed PMID: 14985441.
998 25. Perdomini M, Hick A, Puccio H, Pook MA. Animal and cellular models of Friedreich ataxia.
999 Journal of neurochemistry. 2013 Aug;126 Suppl 1:65-79. PubMed PMID: 23859342.
000 26. Metz G, Coppard N, Cooper JM, Delatycki MB, Durr A, Di Prospero NA, Giunti P, Lynch DR,
001 Schulz JB, Rummey C, Meier T. Rating disease progression of Friedreich's ataxia by the International

002 Cooperative Ataxia Rating Scale: analysis of a 603-patient database. Brain : a journal of neurology.
003 2013 Jan;136(Pt 1):259-68. PubMed PMID: 23365101. Pubmed Central PMCID: 3624678.
004 27. Nakashima Y, Yanez DA, Touma M, Nakano H, Jaroszewicz A, Jordan MC, Pellegrini M, Roos
005 KP, Nakano A. Nkx2-5 suppresses the proliferation of atrial myocytes and conduction system.
006 Circulation research. 2014 Mar 28;114(7):1103-13. PubMed PMID: 24563458.
007 28. Seibler J, Kleinridders A, Kuter-Luks B, Niehaves S, Bruning JC, Schwenk F. Reversible gene
008 knockdown in mice using a tight, inducible shRNA expression system. Nucleic acids research.
009 2007;35(7):e54. PubMed PMID: 17376804. Pubmed Central PMCID: 1874634.
010 29. Crawley JN. What's wrong with my mouse? : behavioral phenotyping of transgenic and knockout
011 mice. 2nd ed. Hoboken, N.J.: Wiley-Interscience; 2007. xvi, 523 p. p.
012 30. Dellon ES, Dellon AL. Functional assessment of neurologic impairment: track analysis in
013 diabetic and compression neuropathies. Plastic and reconstructive surgery. 1991 Oct;88(4):686-94.
014 PubMed PMID: 1896540.
015 31. Tsou AY, Paulsen EK, Lagedrost SJ, Perlman SL, Mathews KD, Wilmot GR, Ravina B,
016 Koeppen AH, Lynch DR. Mortality in Friedreich ataxia. Journal of the neurological sciences. 2011 Aug
017 15;307(1-2):46-9. PubMed PMID: 21652007.
018 32. Smyth GK. limma: Linear Models for Microarray Data. In: Gentleman R, Carey VJ, Huber W,
019 Irizarry RA, Dudoit S, editors. Bioinformatics and Computational Biology Solutions Using R and
020 Bioconductor. New York, NY: Springer New York; 2005. p. 397-420.
021 33. Surawicz B, Knoebel SB. Long QT: good, bad or indifferent? Journal of the American College
022 of Cardiology. 1984 Aug;4(2):398-413. PubMed PMID: 6145737.
023 34. German DM, Kabir MM, Dewland TA, Henrikson CA, Tereshchenko LG. Atrial Fibrillation
024 Predictors: Importance of the Electrocardiogram. Annals of noninvasive electrocardiology : the official
025 journal of the International Society for Holter and Noninvasive Electrocardiology, Inc. 2016
026 Jan;21(1):20-9. PubMed PMID: 26523405. Pubmed Central PMCID: 4728003.
027 35. Dutka DP, Donnelly JE, Nihoyannopoulos P, Oakley CM, Nunez DJ. Marked variation in the
028 cardiomyopathy associated with Friedreich's ataxia. Heart. 1999 Feb;81(2):141-7. PubMed PMID:
029 9922348. Pubmed Central PMCID: 1728941.
030 36. Isnard R, Kalotka H, Durr A, Cossee M, Schmitt M, Pousset F, Thomas D, Brice A, Koenig M,
031 Komajda M. Correlation between left ventricular hypertrophy and GAA trinucleotide repeat length in
032 Friedreich's ataxia. Circulation. 1997 May 06;95(9):2247-9. PubMed PMID: 9142000.
033 37. Durr A, Cossee M, Agid Y, Campuzano V, Mignard C, Penet C, Mandel JL, Brice A, Koenig M.
034 Clinical and genetic abnormalities in patients with Friedreich's ataxia. The New England journal of
035 medicine. 1996 Oct 17;335(16):1169-75. PubMed PMID: 8815938.
036 38. Conrad CH, Brooks WW, Hayes JA, Sen S, Robinson KG, Bing OH. Myocardial fibrosis and
037 stiffness with hypertrophy and heart failure in the spontaneously hypertensive rat. Circulation. 1995 Jan
038 1;91(1):161-70. PubMed PMID: 7805198.
039 39. Bradley JL, Blake JC, Chamberlain S, Thomas PK, Cooper JM, Schapira AH. Clinical,
040 biochemical and molecular genetic correlations in Friedreich's ataxia. Human molecular genetics. 2000
041 Jan 22;9(2):275-82. PubMed PMID: 10607838.
042 40. Rotig A, de Lonlay P, Chretien D, Foury F, Koenig M, Sidi D, Munnich A, Rustin P. Aconitase
043 and mitochondrial iron-sulphur protein deficiency in Friedreich ataxia. Nature genetics. 1997
044 Oct;17(2):215-7. PubMed PMID: 9326946.
045 41. Seyer LA, Galetta K, Wilson J, Sakai R, Perlman S, Mathews K, Wilmot GR, Gomez CM,
046 Ravina B, Zesiewicz T, Bushara KO, Subramony SH, Ashizawa T, Delatycki MB, Brocht A, Balcer LJ,

047 Lynch DR. Analysis of the visual system in Friedreich ataxia. Journal of neurology. 2013
048 Sep;260(9):2362-9. PubMed PMID: 23775342.
049 42. Fortuna F, Barboni P, Liguori R, Valentino ML, Savini G, Gellera C, Mariotti C, Rizzo G,
050 Tonon C, Manners D, Lodi R, Sadun AA, Carelli V. Visual system involvement in patients with
051 Friedreich's ataxia. Brain : a journal of neurology. 2009 Jan;132(Pt 1):116-23. PubMed PMID:
052 18931386.
053 43. Saxena S, Srivastav K, Cheung CM, Ng JY, Lai TY. Photoreceptor inner segment ellipsoid band
054 integrity on spectral domain optical coherence tomography. Clinical ophthalmology. 2014;8:2507-22.
055 PubMed PMID: 25525329. Pubmed Central PMCID: 4266419.
056 44. Coppola G, Burnett R, Perlman S, Versano R, Gao F, Plasterer H, Rai M, Sacca F, Filla A,
057 Lynch DR, Rusche JR, Gottesfeld JM, Pandolfo M, Geschwind DH. A gene expression phenotype in
058 lymphocytes from Friedreich ataxia patients. Annals of neurology. 2011 Nov;70(5):790-804. PubMed
059 PMID: 22162061. Pubmed Central PMCID: 3646419.
060 45. Cartier L, Hartley O, Dubois-Dauphin M, Krause KH. Chemokine receptors in the central
061 nervous system: role in brain inflammation and neurodegenerative diseases. Brain research Brain
062 research reviews. 2005 Feb;48(1):16-42. PubMed PMID: 15708626.
063 46. Leszek J, Barreto GE, Gasiorowski K, Koutsouraki E, Avila-Rodrigues M, Aliev G.
064 Inflammatory Mechanisms and Oxidative Stress as Key Factors Responsible for Progression of
065 Neurodegeneration: Role of Brain Innate Immune System. CNS & neurological disorders drug targets.
066 2016;15(3):329-36. PubMed PMID: 26831258.
067 47. Fung TC, Olson CA, Hsiao EY. Interactions between the microbiota, immune and nervous
068 systems in health and disease. Nature neuroscience. 2017 Jan 16. PubMed PMID: 28092661.
069 48. Andreasson KI, Bachstetter AD, Colonna M, Ginhoux F, Holmes C, Lamb B, Landreth G, Lee
070 DC, Low D, Lynch MA, Monsonego A, O'Banion MK, Pekny M, Puschmann T, Russek-Blum N,
071 Sandusky LA, Selenica ML, Takata K, Teeling J, Town T, Van Eldik LJ. Targeting innate immunity for
072 neurodegenerative disorders of the central nervous system. Journal of neurochemistry. 2016
073 Sep;138(5):653-93. PubMed PMID: 27248001.
074 49. Zhang B, Horvath S. A general framework for weighted gene co-expression network analysis.
075 Statistical applications in genetics and molecular biology. 2005;4:Article17. PubMed PMID: 16646834.
076 50. Langfelder P, Horvath S. WGCNA: an R package for weighted correlation network analysis.
077 BMC bioinformatics. 2008;9:559. PubMed PMID: 19114008. Pubmed Central PMCID: 2631488.
078 51. Geschwind DH, Konopka G. Neuroscience in the era of functional genomics and systems
079 biology. Nature. 2009 Oct 15;461(7266):908-15. PubMed PMID: 19829370. Pubmed Central PMCID:
080 3645852.
081 52. Zhang B, Gaiteri C, Bodea LG, Wang Z, McElwee J, Podtelezhnikov AA, Zhang C, Xie T, Tran
082 L, Dobrin R, Fluder E, Clurman B, Melquist S, Narayanan M, Suver C, Shah H, Mahajan M, Gillis T,
083 Mysore J, MacDonald ME, Lamb JR, Bennett DA, Molony C, Stone DJ, Gudnason V, Myers AJ, Schadt
084 EE, Neumann H, Zhu J, Emilsson V. Integrated systems approach identifies genetic nodes and networks
085 in late-onset Alzheimer's disease. Cell. 2013 Apr 25;153(3):707-20. PubMed PMID: 23622250. Pubmed
086 Central PMCID: 3677161.
087 53. Parikshak NN, Swarup V, Belgard TG, Irimia M, Ramaswami G, Gandal MJ, Hartl C, Leppa V,
088 Ubieta LT, Huang J, Lowe JK, Blencowe BJ, Horvath S, Geschwind DH. Genome-wide changes in
089 lncRNA, splicing, and regional gene expression patterns in autism. Nature. 2016 Dec 05. PubMed
090 PMID: 27919067.

091 54. Haugen AC, Di Prospero NA, Parker JS, Fannin RD, Chou J, Meyer JN, Halweg C, Collins JB,
092 Durr A, Fischbeck K, Van Houten B. Altered gene expression and DNA damage in peripheral blood
093 cells from Friedreich's ataxia patients: cellular model of pathology. PLoS genetics. 2010 Jan
094 15;6(1):e1000812. PubMed PMID: 20090835. Pubmed Central PMCID: 2799513.
095 55. Aiyaz M, Lupton MK, Proitsi P, Powell JF, Lovestone S. Complement activation as a biomarker
096 for Alzheimer's disease. Immunobiology. 2012 Feb;217(2):204-15. PubMed PMID: 21856034.
097 56. Risgaard B, Jabbari R, Refsgaard L, Holst AG, Haunso S, Sadjadieh A, Winkel BG, Olesen MS,
098 Tfelt-Hansen J. High prevalence of genetic variants previously associated with Brugada syndrome in
099 new exome data. Clinical genetics. 2013 Nov;84(5):489-95. PubMed PMID: 23414114.
100 57. Bienengraeber M, Olson TM, Selivanov VA, Kathmann EC, O'Cochlain F, Gao F, Karger AB,
101 Ballew JD, Hodgson DM, Zingman LV, Pang YP, Alekseev AE, Terzic A. ABCC9 mutations identified
102 in human dilated cardiomyopathy disrupt catalytic KATP channel gating. Nature genetics. 2004
103 Apr;36(4):382-7. PubMed PMID: 15034580. Pubmed Central PMCID: 1995438.
104 58. Singh VP, Rubinstein J, Arvanitis DA, Ren X, Gao X, Haghighi K, Gilbert M, Iyer VR, Kim
105 DH, Cho C, Jones K, Lorenz JN, Armstrong CF, Wang HS, Gyorke S, Kranias EG. Abnormal calcium
106 cycling and cardiac arrhythmias associated with the human Ser96Ala genetic variant of histidine-rich
107 calcium-binding protein. Journal of the American Heart Association. 2013 Oct 14;2(5):e000460.
108 PubMed PMID: 24125847. Pubmed Central PMCID: 3835262.
109 59. Gonzalez A, Fortuno MA, Querejeta R, Ravassa S, Lopez B, Lopez N, Diez J. Cardiomyocyte
110 apoptosis in hypertensive cardiomyopathy. Cardiovascular research. 2003 Sep 01;59(3):549-62. PubMed
111 PMID: 14499856.
112 60. Huang ML, Becker EM, Whitnall M, Suryo Rahmanto Y, Ponka P, Richardson DR. Elucidation
113 of the mechanism of mitochondrial iron loading in Friedreich's ataxia by analysis of a mouse mutant.
114 Proceedings of the National Academy of Sciences of the United States of America. 2009 Sep
115 22;106(38):16381-6. PubMed PMID: 19805308. Pubmed Central PMCID: 2752539.
116 61. Bolinches-Amoros A, Molla B, Pla-Martin D, Palau F, Gonzalez-Cabo P. Mitochondrial
117 dysfunction induced by frataxin deficiency is associated with cellular senescence and abnormal calcium
118 metabolism. Frontiers in cellular neuroscience. 2014;8:124. PubMed PMID: 24860428. Pubmed Central
119 PMCID: 4026758.
120 62. Muzio M, Chinnaiyan AM, Kischkel FC, O'Rourke K, Shevchenko A, Ni J, Scaffidi C, Bretz JD,
121 Zhang M, Gentz R, Mann M, Krammer PH, Peter ME, Dixit VM. FLICE, a novel FADD-homologous
122 ICE/CED-3-like protease, is recruited to the CD95 (Fas/APO-1) death--inducing signaling complex.
123 Cell. 1996 Jun 14;85(6):817-27. PubMed PMID: 8681377.
124 63. Kyrylkova K, Kyryachenko S, Leid M, Kioussi C. Detection of apoptosis by TUNEL assay.
125 Methods in molecular biology. 2012;887:41-7. PubMed PMID: 22566045.
126 64. Trugenberger CA, Walti C, Peregrim D, Sharp ME, Bureeva S. Discovery of novel biomarkers
127 and phenotypes by semantic technologies. BMC bioinformatics. 2013 Feb 13;14:51. PubMed PMID:
128 23402646. Pubmed Central PMCID: 3605201.
129 65. Vermeer S, Hoischen A, Meijer RP, Gilissen C, Neveling K, Wieskamp N, de Brouwer A,
130 Koenig M, Anheim M, Assoum M, Drouot N, Todorovic S, Milic-Rasic V, Lochmuller H, Stevanin G,
131 Goizet C, David A, Durr A, Brice A, Kremer B, van de Warrenburg BP, Schijvenaars MM, Heister A,
132 Kwint M, Arts P, van der Wijst J, Veltman J, Kamsteeg EJ, Scheffer H, Knoers N. Targeted next-
133 generation sequencing of a 12.5 Mb homozygous region reveals ANO10 mutations in patients with
134 autosomal-recessive cerebellar ataxia. American journal of human genetics. 2010 Dec 10;87(6):813-9.
135 PubMed PMID: 21092923. Pubmed Central PMCID: 2997370.

136 66. Miskovic ND, Domingo A, Dobricic V, Max C, Braenne I, Petrovic I, Grutz K, Pawlack H,
137 Tournev I, Kalaydjieva L, Svetel M, Lohmann K, Kostic VS, Westenberger A. Seemingly dominant
138 inheritance of a recessive ANO10 mutation in romani families with cerebellar ataxia. Movement
139 disorders : official journal of the Movement Disorder Society. 2016 Oct 27. PubMed PMID: 27787937.
140 67. Mollet J, Delahodde A, Serre V, Chretien D, Schlemmer D, Lombes A, Boddaert N, Desguerre I,
141 de Lonlay P, de Baulny HO, Munnich A, Rotig A. CABC1 gene mutations cause ubiquinone deficiency
142 with cerebellar ataxia and seizures. American journal of human genetics. 2008 Mar;82(3):623-30.
143 PubMed PMID: 18319072. Pubmed Central PMCID: 2427298.
144 68. Gerards M, van den Bosch B, Calis C, Schoonderwoerd K, van Engelen K, Tijssen M, de Coo R,
145 van der Kooi A, Smeets H. Nonsense mutations in CABC1/ADCK3 cause progressive cerebellar ataxia
146 and atrophy. Mitochondrion. 2010 Aug;10(5):510-5. PubMed PMID: 20580948.
147 69. Schicks J, Synofzik M, Schulte C, Schols L. POLG, but not PEO1, is a frequent cause of
148 cerebellar ataxia in Central Europe. Movement disorders : official journal of the Movement Disorder
149 Society. 2010 Nov 15;25(15):2678-82. PubMed PMID: 20803511.
150 70. Synofzik M, Srulijes K, Godau J, Berg D, Schols L. Characterizing POLG ataxia: clinics,
151 electrophysiology and imaging. Cerebellum. 2012 Dec;11(4):1002-11. PubMed PMID: 22528963.
152 71. Pennacchio LA, Bouley DM, Higgins KM, Scott MP, Noebels JL, Myers RM. Progressive
153 ataxia, myoclonic epilepsy and cerebellar apoptosis in cystatin B-deficient mice. Nature genetics. 1998
154 Nov;20(3):251-8. PubMed PMID: 9806543.
155 72. Singh S, Ganesh S. Lafora progressive myoclonus epilepsy: a meta-analysis of reported
156 mutations in the first decade following the discovery of the EPM2A and NHLRC1 genes. Human
157 mutation. 2009 May;30(5):715-23. PubMed PMID: 19267391.
158 73. Matthijs G, Schollen E, Pardon E, Veiga-Da-Cunha M, Jaeken J, Cassiman JJ, Van Schaftingen
159 E. Mutations in PMM2, a phosphomannomutase gene on chromosome 16p13, in carbohydrate-deficient
160 glycoprotein type I syndrome (Jaeken syndrome). Nature genetics. 1997 May;16(1):88-92. PubMed
161 PMID: 9140401.
162 74. Sygitowicz G, Tomaniak M, Filipiak KJ, Koltowski L, Sitkiewicz D. Galectin-3 in Patients with
163 Acute Heart Failure: Preliminary Report on First Polish Experience. Advances in clinical and
164 experimental medicine : official organ Wroclaw Medical University. 2016 Jul-Aug;25(4):617-23.
165 PubMed PMID: 27629834.
166 75. Salvador AM, Nevers T, Velazquez F, Aronovitz M, Wang B, Abadia Molina A, Jaffe IZ, Karas
167 RH, Blanton RM, Alcaide P. Intercellular Adhesion Molecule 1 Regulates Left Ventricular Leukocyte
168 Infiltration, Cardiac Remodeling, and Function in Pressure Overload-Induced Heart Failure. Journal of
169 the American Heart Association. 2016 Mar 15;5(3):e003126. PubMed PMID: 27068635. Pubmed
170 Central PMCID: 4943280.
171 76. Polyakova V, Loeffler I, Hein S, Miyagawa S, Piotrowska I, Dammer S, Risteli J, Schaper J,
172 Kostin S. Fibrosis in endstage human heart failure: severe changes in collagen metabolism and
173 MMP/TIMP profiles. International journal of cardiology. 2011 Aug 18;151(1):18-33. PubMed PMID:
174 20546954.
175 77. Del-Castillo-Rueda A, Moreno-Carralero MI, Cuadrado-Grande N, Alvarez-Sala-Walther LA,
176 Enriquez-de-Salamanca R, Mendez M, Moran-Jimenez MJ. Mutations in the HFE, TFR2, and SLC40A1
177 genes in patients with hemochromatosis. Gene. 2012 Oct 15;508(1):15-20. PubMed PMID: 22890139.
178 78. Song W, Zukor H, Lin SH, Liberman A, Tavitian A, Mui J, Vali H, Fillebeen C, Pantopoulos K,
179 Wu TD, Guerquin-Kern JL, Schipper HM. Unregulated brain iron deposition in transgenic mice over-

180 expressing HMOX1 in the astrocytic compartment. Journal of neurochemistry. 2012 Oct;123(2):325-36.
181 PubMed PMID: 22881289.
182 79. Cui R, Gale RP, Zhu G, Xu Z, Qin T, Zhang Y, Huang G, Li B, Fang L, Zhang H, Pan L, Hu N,
183 Qu S, Xiao Z. Serum iron metabolism and erythropoiesis in patients with myelodysplastic syndrome not
184 receiving RBC transfusions. Leukemia research. 2014 May;38(5):545-50. PubMed PMID: 24598841.
185 Pubmed Central PMCID: 4439195.
186 80. Pavel M, Rubinsztein DC. Mammalian autophagy and the plasma membrane. The FEBS journal.
187 2016 Oct 18. PubMed PMID: 27758042.
188 81. Bento CF, Renna M, Ghislat G, Puri C, Ashkenazi A, Vicinanza M, Menzies FM, Rubinsztein
189 DC. Mammalian Autophagy: How Does It Work? Annual review of biochemistry. 2016 Jun 02;85:685-
190 713. PubMed PMID: 26865532.
191 82. Gustafsson AB, Gottlieb RA. Autophagy in ischemic heart disease. Circulation research. 2009
192 Jan 30;104(2):150-8. PubMed PMID: 19179668. Pubmed Central PMCID: 2765251.
193 83. Perdomini M, Belbellaa B, Monassier L, Reutenauer L, Messaddeq N, Cartier N, Crystal RG,
194 Aubourg P, Puccio H. Prevention and reversal of severe mitochondrial cardiomyopathy by gene therapy
195 in a mouse model of Friedreich's ataxia. Nature medicine. 2014 May;20(5):542-7. PubMed PMID:
196 24705334.
197 84. Gottesfeld JM, Rusche JR, Pandolfo M. Increasing frataxin gene expression with histone
198 deacetylase inhibitors as a therapeutic approach for Friedreich's ataxia. Journal of neurochemistry. 2013
199 Aug;126 Suppl 1:147-54. PubMed PMID: 23859350. Pubmed Central PMCID: 3766837.
200 85. Delatycki MB, Camakaris J, Brooks H, Evans-Whipp T, Thorburn DR, Williamson R, Forrest
201 SM. Direct evidence that mitochondrial iron accumulation occurs in Friedreich ataxia. Annals of
202 neurology. 1999 May;45(5):673-5. PubMed PMID: 10319894.
203 86. Michael S, Petrocine SV, Qian J, Lamarche JB, Knutson MD, Garrick MD, Koeppen AH. Iron
204 and iron-responsive proteins in the cardiomyopathy of Friedreich's ataxia. Cerebellum. 2006;5(4):257-
205 67. PubMed PMID: 17134988.
206 87. Lynch DR, Deutsch EC, Wilson RB, Tennekoon G. Unanswered questions in Friedreich ataxia.
207 Journal of child neurology. 2012 Sep;27(9):1223-9. PubMed PMID: 22832776. Pubmed Central
208 PMCID: 3674553.
209 88. Fujita T, Ishikawa Y. Apoptosis in heart failure. -The role of the beta-adrenergic receptor-
210 mediated signaling pathway and p53-mediated signaling pathway in the apoptosis of cardiomyocytes.
211 Circulation journal : official journal of the Japanese Circulation Society. 2011;75(8):1811-8. PubMed
212 PMID: 21747195.
213 89. Bennett MR. Apoptosis in the cardiovascular system. Heart. 2002 May;87(5):480-7. PubMed
214 PMID: 11997428. Pubmed Central PMCID: 1767116.
215 90. Ravichandran KS. Beginnings of a good apoptotic meal: the find-me and eat-me signaling
216 pathways. Immunity. 2011 Oct 28;35(4):445-55. PubMed PMID: 22035837. Pubmed Central PMCID:
217 3241945.
218 91. Martinet W, Knaapen MW, Kockx MM, De Meyer GR. Autophagy in cardiovascular disease.
219 Trends in molecular medicine. 2007 Nov;13(11):482-91. PubMed PMID: 18029229.
220 92. Eisenberg-Lerner A, Bialik S, Simon HU, Kimchi A. Life and death partners: apoptosis,
221 autophagy and the cross-talk between them. Cell death and differentiation. 2009 Jul;16(7):966-75.
222 PubMed PMID: 19325568.

93. Tan G, Chen LS, Lonnerdal B, Gellera C, Taroni FA, Cortopassi GA. Frataxin expression rescues mitochondrial dysfunctions in FRDA cells. Human molecular genetics. 2001 Sep 15;10(19):2099-107. PubMed PMID: 11590127.
94. Koutnikova H, Campuzano V, Foury F, Dolle P, Cazzalini O, Koenig M. Studies of human, mouse and yeast homologues indicate a mitochondrial function for frataxin. Nature genetics. 1997 Aug;16(4):345-51. PubMed PMID: 9241270.
95. Foury F, Cazzalini O. Deletion of the yeast homologue of the human gene associated with Friedreich's ataxia elicits iron accumulation in mitochondria. FEBS letters. 1997 Jul 14;411(2-3):373-7. PubMed PMID: 9271239.
96. Lodi R, Cooper JM, Bradley JL, Manners D, Styles P, Taylor DJ, Schapira AH. Deficit of in vivo mitochondrial ATP production in patients with Friedreich ataxia. Proceedings of the National Academy of Sciences of the United States of America. 1999 Sep 28;96(20):11492-5. PubMed PMID: 10500204. Pubmed Central PMCID: 18061.
97. Gonzalez-Cabo P, Palau F. Mitochondrial pathophysiology in Friedreich's ataxia. Journal of neurochemistry. 2013 Aug;126 Suppl 1:53-64. PubMed PMID: 23859341.
98. Chan DC. Fusion and fission: interlinked processes critical for mitochondrial health. Annual review of genetics. 2012;46:265-87. PubMed PMID: 22934639.
99. Desagher S, Martinou JC. Mitochondria as the central control point of apoptosis. Trends in cell biology. 2000 Sep;10(9):369-77. PubMed PMID: 10932094.
100. Goodman JM. The gregarious lipid droplet. The Journal of biological chemistry. 2008 Oct 17;283(42):28005-9. PubMed PMID: 18611863. Pubmed Central PMCID: 2568941.
101. Tarnopolsky MA, Rennie CD, Robertshaw HA, Fedak-Tarnopolsky SN, Devries MC, Hamadeh MJ. Influence of endurance exercise training and sex on intramyocellular lipid and mitochondrial ultrastructure, substrate use, and mitochondrial enzyme activity. American journal of physiology Regulatory, integrative and comparative physiology. 2007 Mar;292(3):R1271-8. PubMed PMID: 17095651.
102. Vyas PM, Tomamichel WJ, Pride PM, Babbey CM, Wang Q, Mercier J, Martin EM, Payne RM. A TAT-frataxin fusion protein increases lifespan and cardiac function in a conditional Friedreich's ataxia mouse model. Human molecular genetics. 2012 Mar 15;21(6):1230-47. PubMed PMID: 22113996. Pubmed Central PMCID: 3284115.
103. Rufini A, Cavallo F, Condo I, Fortuni S, De Martino G, Incani O, Di Venere A, Benini M, Massaro DS, Arcuri G, Serio D, Malisan F, Testi R. Highly specific ubiquitin-competing molecules effectively promote frataxin accumulation and partially rescue the aconitase defect in Friedreich ataxia cells. Neurobiology of disease. 2015 Mar;75:91-9. PubMed PMID: 25549872. Pubmed Central PMCID: 4358773.
104. Coppola G, Choi SH, Santos MM, Miranda CJ, Tentler D, Wexler EM, Pandolfo M, Geschwind DH. Gene expression profiling in frataxin deficient mice: microarray evidence for significant expression changes without detectable neurodegeneration. Neurobiology of disease. 2006 May;22(2):302-11. PubMed PMID: 16442805. Pubmed Central PMCID: 2886035.
105. Shen Y, McMackin MZ, Shan Y, Raetz A, David S, Cortopassi G. Frataxin Deficiency Promotes Excess Microglial DNA Damage and Inflammation that Is Rescued by PJ34. PloS one. 2016;11(3):e0151026. PubMed PMID: 26954031. Pubmed Central PMCID: 4783034.
106. Lu C, Schoenfeld R, Shan Y, Tsai HJ, Hammock B, Cortopassi G. Frataxin deficiency induces Schwann cell inflammation and death. Biochimica et biophysica acta. 2009 Nov;1792(11):1052-61. PubMed PMID: 19679182. Pubmed Central PMCID: 3563672.

107. Strawser CJ, Schadt KA, Lynch DR. Therapeutic approaches for the treatment of Friedreich's ataxia. Expert review of neurotherapeutics. 2014 Aug;14(8):949-57. PubMed PMID: 25034024.

108. Sandi C, Sandi M, Anjomani Virmouni S, Al-Mahdawi S, Pook MA. Epigenetic-based therapies for Friedreich ataxia. Frontiers in genetics. 2014;5:165. PubMed PMID: 24917884. Pubmed Central PMCID: 4042889.

109. Kearney M, Orrell RW, Fahey M, Brassington R, Pandolfo M. Pharmacological treatments for Friedreich ataxia. The Cochrane database of systematic reviews. 2016 Aug 30(8):CD007791. PubMed PMID: 27572719.

110. Oldham MC, Horvath S, Geschwind DH. Conservation and evolution of gene coexpression networks in human and chimpanzee brains. Proceedings of the National Academy of Sciences of the United States of America. 2006 Nov 21;103(47):17973-8. PubMed PMID: 17101986. Pubmed Central PMCID: 1693857.

111. Langfelder P, Horvath S. Eigengene networks for studying the relationships between co-expression modules. BMC systems biology. 2007;1:54. PubMed PMID: 18031580. Pubmed Central PMCID: 2267703.

112. Huang da W, Sherman BT, Lempicki RA. Systematic and integrative analysis of large gene lists using DAVID bioinformatics resources. Nature protocols. 2009;4(1):44-57. PubMed PMID: 19131956.

113. Becker KG, Hosack DA, Dennis G, Jr., Lempicki RA, Bright TJ, Cheadle C, Engel J. PubMatrix: a tool for multiplex literature mining. BMC bioinformatics. 2003 Dec 10;4:61. PubMed PMID: 14667255. Pubmed Central PMCID: 317283.

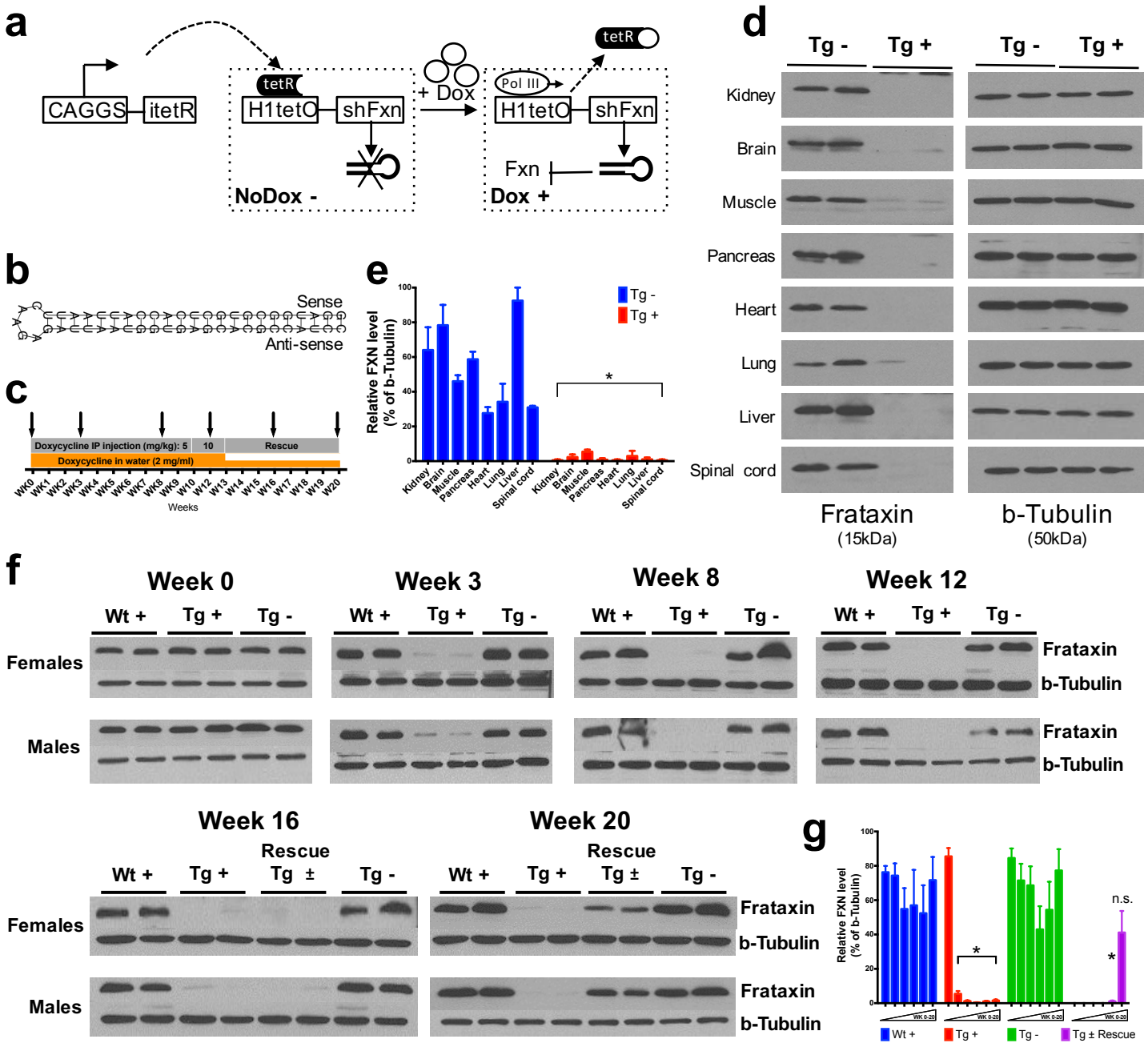
a
CAGGS
itetR
tetR
H1tetO
shFxn
NoDox -
+ Dox
Pol III
tetR
H1tetO
shFxn
Fxn
Dox +
b
Sense
Anti-sense
c
Doxycycline IP injection (mg/kg): 5
10
Rescue
Doxycycline in water (2 mg/ml)
Weeks
e
Relative FXN level (% of b-Tubulin)
Tg -
Tg +
Kidney
Brain
Muscle
Pancreas
Heart
Lung
Liver
Spinal cord
d
Tg -
Tg +
Kidney
Brain
Muscle
Pancreas
Heart
Lung
Liver
Spinal cord
Frataxin
(15kDa)
b-Tubulin
(50kDa)
f
Week 0
Week 3
Week 8
Week 12
Wt +
Tg +
Tg -
Females
Males
Frataxin
b-Tubulin
Week 16
Week 20
Rescue
Tg ±
g
Relative FXN level (% of b-Tubulin)
n.s.
Wt +
Tg +
Tg -
Tg ± Rescue

Figure 1

Figure 1: Efficient temporal in vivo frataxin knockdown and rescue. (**a**) Schematic representation of the inducible vector system to mediated expression of shRNA expression against frataxin. The vector contains shRNA sequence against frataxin (*Fxn*) gene regulated by the H1 promoter with tet-operator sequences (tetO) and tet repressor (tetR) under the control of the CAGGS promoter. Transcription of the *Fxn* shRNA is blocked in cells expressing the tetR. Upon induction by doxycycline (dox), tetR is removed from the tetO sequences inserted into the promoter, allowing transcription of shRNA against *Fxn*. shRNA expression leads to RNAi-mediated knockdown of *Fxn* gene. (**b**) Predicted minimum free energy secondary structure of expressed shRNA targeting the *Fxn* is shown with the sequence (sense strand) and its complement sequence (antisense strand) in the duplex form along with hairpin loop. (**c**) Timeline for doxycycline treatment of mice with a double IP injection (5 and 10 mg/kg) of dox per week and in drinking water (2 mg/ml). IP injections and dox in water was withdrawn for rescue animals. Arrow signs indicated different time intervals considered for downstream analyses. (**d**) Transgenic mice without (Tg -) or with (Tg +) doxycycline treatment (see c) for 20 weeks were analyzed by Western blot for protein levels of FXN in various organs. (**e**) For quantification, FXN values were normalized to the level of b-tubulin in each lane. (**f**) Time series FXN knockdown and rescue in liver. Wild-type mice with dox (Wt +), transgenic mice with (Tg +) and without (Tg -) dox, and transgenic mice with (Tg ±) dox removal (rescue) samples were analyzed for week 0,3,8,12,16 and 20. Rescue animals (Tg ±) were given dox for 12 weeks and doxycycline was withdrawn for additional 4 and 8 weeks. (**g**) For quantification, FXN values were normalized to the level of b-tubulin in each lane. N=4 animals per group, *=$p<0.01$; two-way ANOVA test; n.s., not significant. Error bars represent mean ± SEM for panels e and g.

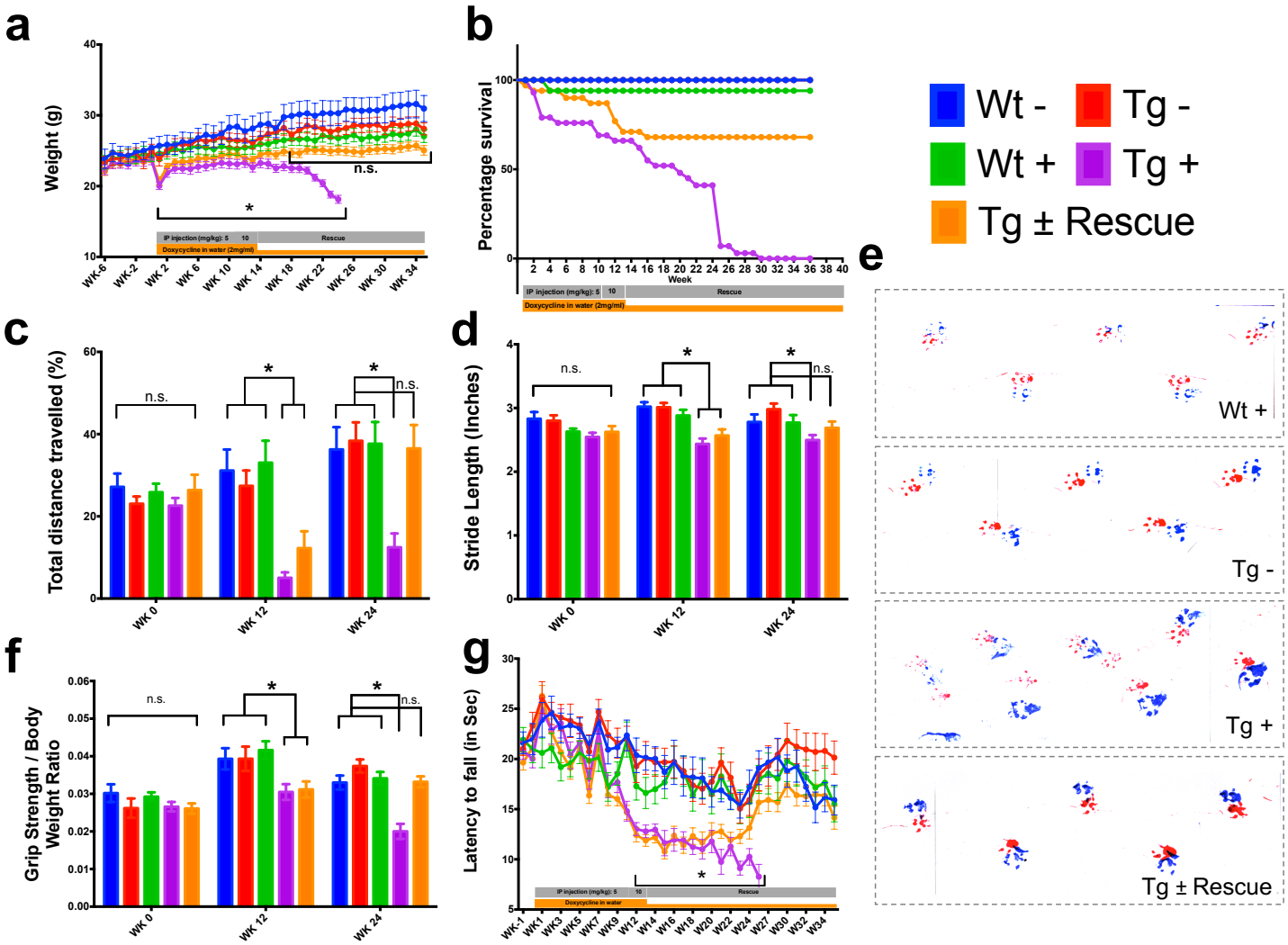
a
Weight (g)
n.s.
*
IP injection (mg/kg): 5 10 Rescue
Doxycycline in water (2mg/ml)
WK-6 WK-2 WK 2 WK 6 WK 10 WK 14 WK 18 WK 22 WK 26 WK 30 WK 34
b
Percentage survival
Week
IP injection (mg/kg): 5 10 Rescue
Doxycycline in water (2mg/ml)
Wt -
Tg -
Wt +
Tg +
Tg ± Rescue
c
Total distance travelled (%)
n.s.
*
*
n.s.
WK 0
WK 12
WK 24
d
Stride Length (Inches)
n.s.
*
*
n.s.
WK 0
WK 12
WK 24
e
Wt +
Tg -
Tg +
Tg ± Rescue
f
Grip Strength / Body Weight Ratio
n.s.
*
*
n.s.
WK 0
WK 12
WK 24
g
Latency to fall (in Sec)
*
IP injection (mg/kg): 5 10 Rescue
Doxycycline in water
WK-1 WK1 WK3 WK5 WK7 WK9 W12 W14 W16 W18 W20 W22 W24 W27 W30 W32 W34

Figure 2

Figure 2: Neurological deficits due to frataxin knockdown. Body weight, survival, open field, gait analysis, grip strength and rotarod in five groups of animals; wild-type mice with dox (Wt +, n= 16(WK 0), n= 16(WK 12), n= 16(WK 24)) and without dox (Wt -, n= 16(WK 0), n= 16(WK 12), n= 16(WK 24)), transgenic mice with dox (Tg +, n= 30(WK 0), n= 21(WK 12), n= 15(WK 24)) and without dox (Tg -, n= 16(WK 0), n= 15(WK 12), n= 15(WK 24)), and transgenic mice with dox removal (Tg ± Rescue, n= 30(WK 0), n= 21(WK 12), n= 20(WK 24)). (**a**) Body weight from before 6 weeks and upto 34 weeks after dox treatment. (**b**) Survival was significantly declined in dox treated Tg + group of animals, no mortality was observed after dox withdrawal (Tg ± Rescue). (**c**) Open field test showing significant decline in total distance traveled by the dox treatment transgenic animals (Tg +) at 12 and 24 weeks when compared across all other groups. After dox withdrawal, there were no differences between the rescue group (Tg ± Rescue) and the three control groups at week 24. (**d**) Gait footprint analysis of all five groups of mice at 0, 12 and 24 weeks was evaluated for stride length. Dox treated transgenic (Tg +) animals revealed abnormalities in walking patterns displaying significantly reduced stride length, however the rescue group (Tg ± Rescue) displayed normal stride length when compared to other groups. (**e**) Representative walking footprint patterns. (**f**) Grip-strength test, dox treated transgenic (Tg +) mice had reduced forelimb grip strength at 12 and 24 weeks when compared across all other groups. After dox withdrawal, there were no significant differences between the rescue group (Tg ± Rescue) and the three control groups at week 24. (**g**) Rotarod test in mice upto 34 weeks after dox treatment. Dox treated transgenic (Tg +) animals stayed less time on the rotarod than the control groups, although after dox withdrawal, there was no significant difference between the rescue group (Tg ± Rescue) and the three control groups. Values between all five groups are shown as mean ± SME. Two-way ANOVA test *=P≤0.001; n.s., not significant.

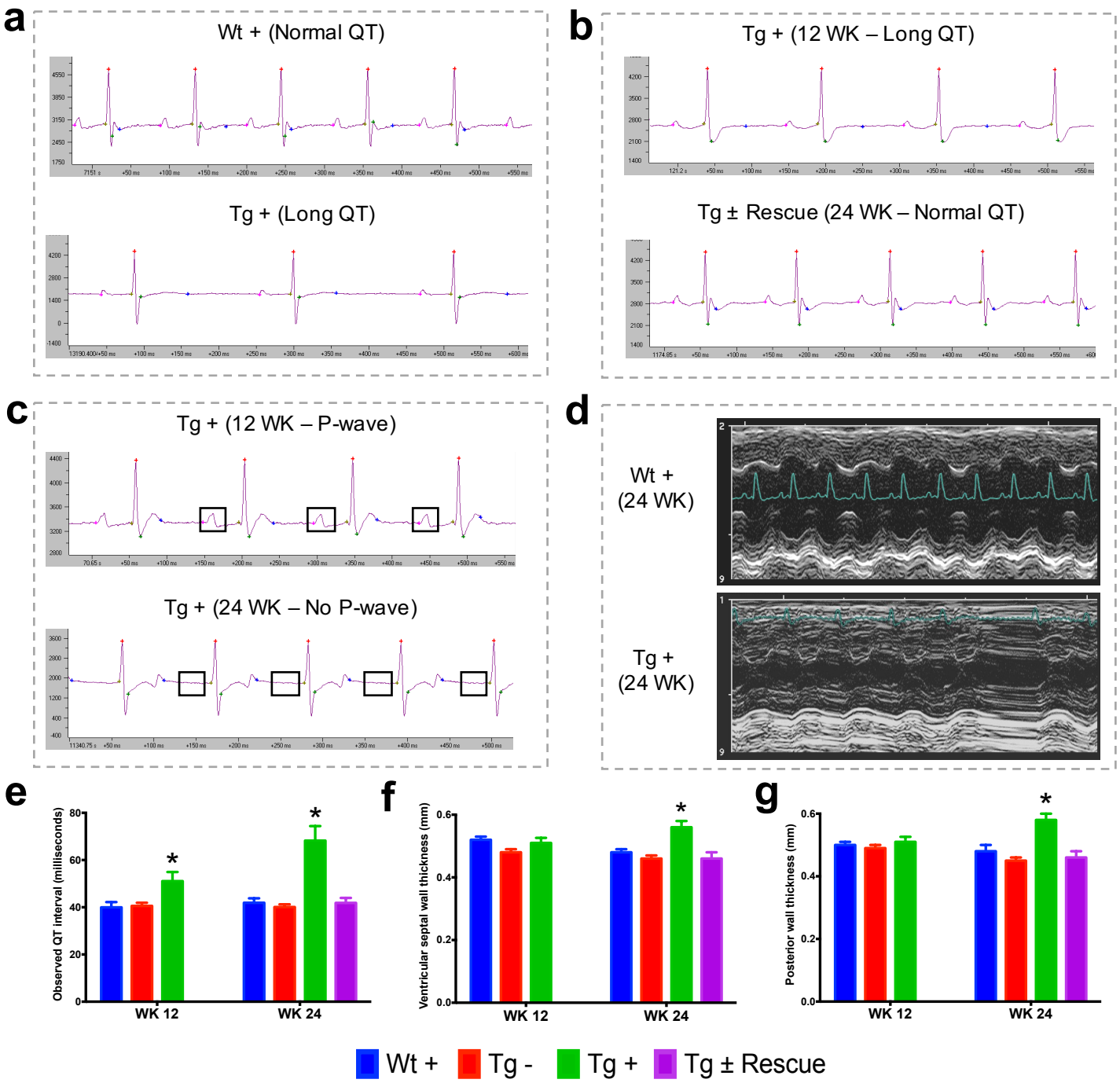
a
Wt + (Normal QT)
Tg + (Long QT)
b
Tg + (12 WK – Long QT)
Tg ± Rescue (24 WK – Normal QT)
c
Tg + (12 WK – P-wave)
Tg + (24 WK – No P-wave)
d
Wt +
(24 WK)
Tg +
(24 WK)
e
Observed QT interval (milliseconds)
WK 12
WK 24
f
Ventricular septal wall thickness (mm)
WK 12
WK 24
g
Posterior wall thickness (mm)
WK 12
WK 24
Wt +
Tg -
Tg +
Tg ± Rescue

Figure 3

Figure 3: Frataxin knockdown mice exhibit signs of cardiomyopathy. (**a**) Representative traces of ECG recording in a wild-type and transgenic animal after dox treatment for 20 weeks, showing long QT intervals in Tg + animal. (**b**) ECG recording of a same dox treated transgenic (Tg +) animal at 12 and after dox withdrawal for additional 12 weeks (Tg ± Rescue), showing normal QT interval. (**c**) ECG recording of a same dox treated transgenic (Tg +) animal at 12 and 24 weeks, showing absences of P-wave only at 24 week. (**d**) Representative echocardiograms from the left ventricle of a wild-type and transgenic mouse at 24 week after dox treatment. (**e-f**) Quantification of observed QT interval (**e**), ventricular septal wall thickness (**f**) and posterior wall thickness (**g**) are shown for week 12 and 24. N = 6-8 animals per group, *=$p<0.05$; Student's t test. Error bars represent mean ± SEM.

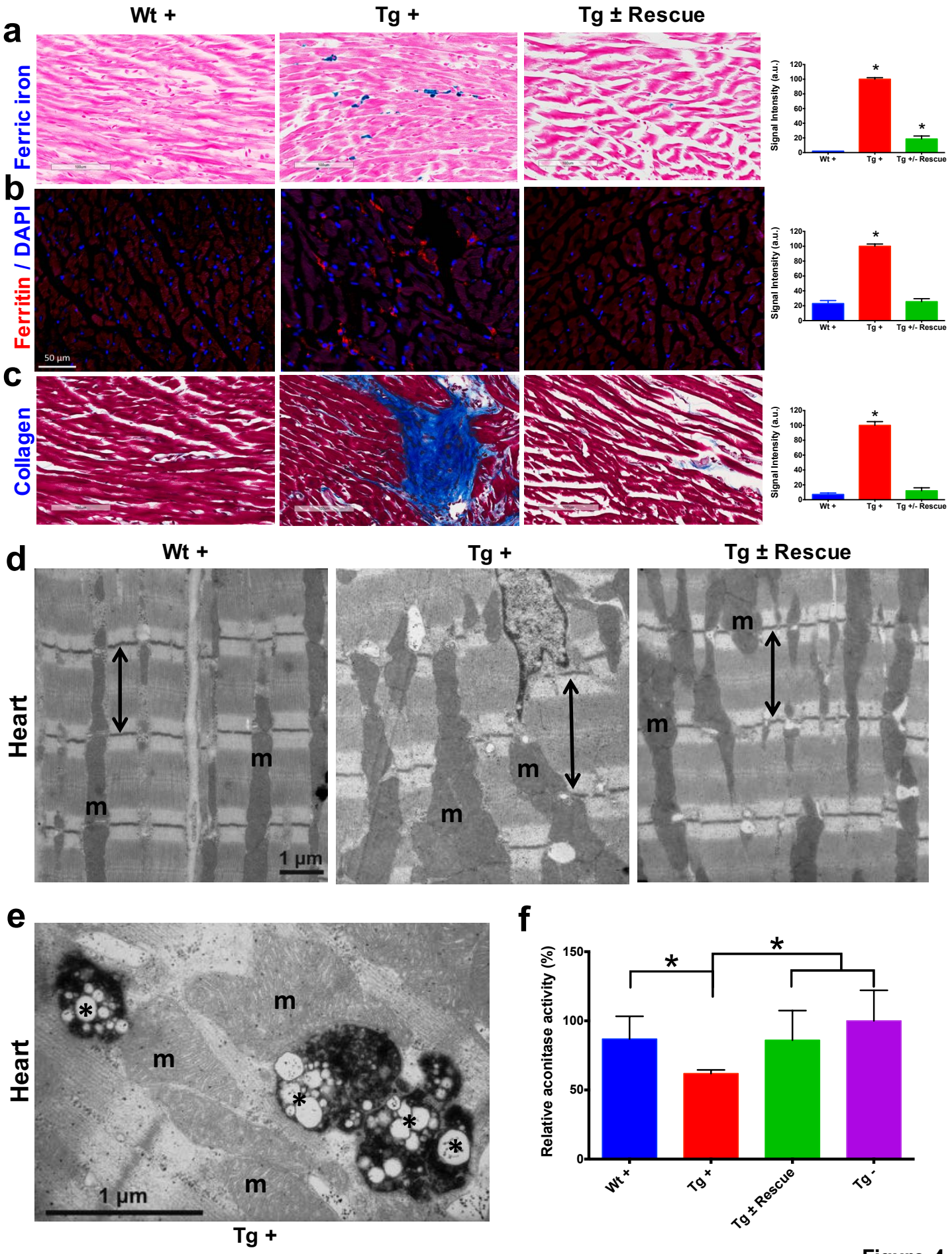
a
Wt +
Tg +
Tg ± Rescue
Ferric iron
Signal Intensity (a.u.)
Wt +
Tg +
Tg +/- Rescue
b
Ferritin / DAPI
50 µm
c
Collagen
d
Heart
m
1 µm
e
Heart
1 µm
Tg +
f
Relative aconitase activity (%)
Wt +
Tg +
Tg ± Rescue
Tg -

Figure 4

Figure 4: Cardiopathology of frataxin knockdown mice. (**a**) Gomori's iron staining and quantification of iron deposition in dox treated transgenic (Tg +), wild-type (Wt +) and dox withdrawn transgenic (Tg ± Rescue) animals. Dox treated transgenic (Tg +) mice showing myocardial iron-overload (a) also displayed altered expression of ferritin protein (**b**) which is involved in iron storage. Both iron-overload and ferritin protein levels were significantly lower in Tg ± Rescue animals (a-b). (**c**) Masson's trichrome staining and quantification showing increased fibrosis in Tg + mice when compared to Wt + and Tg ± Rescue animals. (**d**) Electron micrographs of cardiac muscle from Wt +, Tg + and Tg ± Rescue animals at 20 week after dox treatment. Double arrow lines indicate sarcomere. m = mitochondria. Scale bars, 1 μm. Data are representative of three biological replicates per group. (**e**) Higher magnification of electron micrographs of cardiac muscle from Tg + mice, showing normal (m) and degenerating mitochondria (asterisks). (**f**) Aconitase activity was assayed in triplicate in tissues removed from 3 hearts in each group. Values represent mean ± SME. One-way ANOVA test *=P≤0.05.

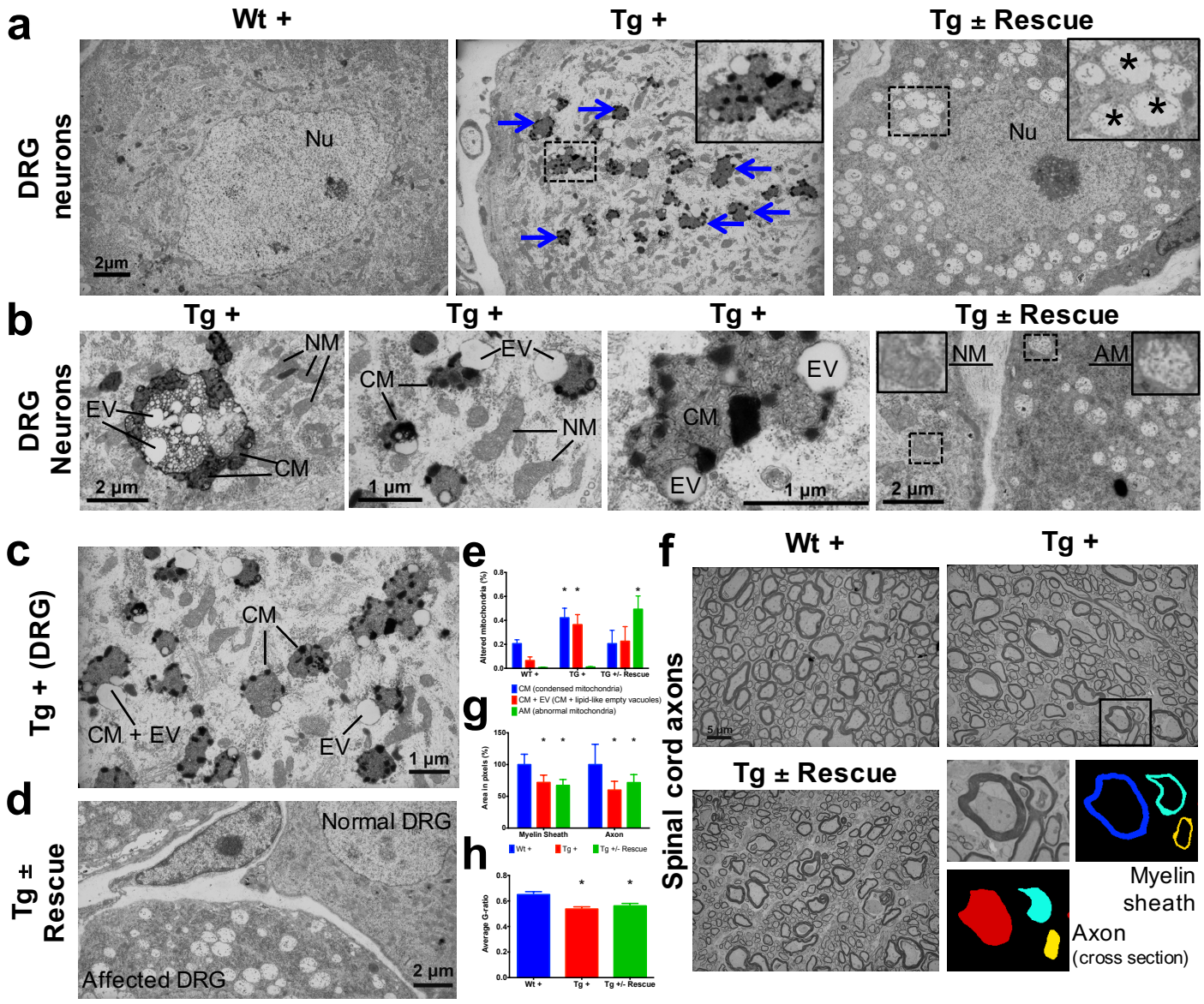
a
Wt +
Tg +
Tg ± Rescue
DRG neurons
Nu
2µm
b
Tg +
Tg ± Rescue
DRG Neurons
NM
EV
CM
AM
2 µm
1 µm
c
Tg + (DRG)
CM
CM + EV
EV
1 µm
d
Tg ± Rescue
Normal DRG
Affected DRG
2 µm
e
Altered mitochondria (%)
WT +
TG +
TG +/- Rescue
CM (condensed mitochondria)
CM + EV (CM + lipid-like empty vacuoles)
AM (abnormal mitochondria)
g
Area in pixels (%)
Myelin Sheath
Axon
Wt +
Tg +
Tg +/- Rescue
h
Average G-ratio
f
Spinal cord axons
5 µm
Myelin sheath
Axon
(cross section)
i
Retina (photoreceptors)
rods and cones
2 µm
j
Retina (RPE cell layer)
RPE layer

Figure 5

Figure 5: Frataxin knockdown mice exhibit neuronal degeneration. (**a**) Electron microscopic analysis of Wt +, Tg + and Tg ± Rescue animal DRG neurons at 20 week after dox treatment. Arrows indicate condensed mitochondria with lipid-like empty vacuoles. Insert in Tg + panel shows higher magnification of electron micrographs of condensed mitochondria with lipid-like empty vacuoles in DRG neurons. Insert in Tg ± Rescue panel shows higher magnification of abnormal mitochondria (asterisks). Nu= nucleus. (**b**) Higher magnification of electron micrographs of Tg + and Tg ± Rescue animal DRG neurons at 20 week after dox treatment. Tg + panel shows degenerating mitochondria and condensed mitochondria with lipid-like empty vacuoles in DRG neurons. Tg ± Rescue panel shows two DRG neurons, one consisting of normal mitochondria (insert) and the other neuron with abnormal mitochondria (insert). (**c**) Higher magnification of Tg + animals showing condensed mitochondria with lipid-like empty vacuoles in DRG neurons. (**d**) Higher magnification of Tg ± rescue animals showing two DRG neurons, one consisting of normal mitochondria (normal DRG) and the other neuron with abnormal mitochondria (affected DRG). NM= normal mitochondria, CM= condensed mitochondria, EV= lipid-like empty vacuoles, AM= abnormal mitochondria. (**e**) Quantification of altered mitochondria in DRG neurons. Data are from multiple images from three biological replicates per group. Values represent mean ± SME. Two-way ANOVA test *=P≤0.05. (**f**) Electron micrographs of spinal cord axon cross-section, displaying reduced myelin sheath thickness and axonal cross-section area in Tg + and Tg ± Rescue animals. Bottom panel shows representative area utilized for quantification. (**g-h**) Quantification of myelin sheath thickness and axonal cross-section area in the spinal cord. Data are from 2000 or more axons per group in the lumbar spinal cord cross-section of high-resolution electron micrographs from three biological replicates per group. Values represent mean ± SME. One-way ANOVA test *=P≤0.05. (**i**) Electron micrographs of rod and cone photoreceptor cells, showing their disruption in Tg + animals (asterisks). (**j**) Retinal pigment epithelium cell layer showing the presences of large vacuoles (arrows) in Tg + animals along with disruption in their photoreceptor cells (asterisks).

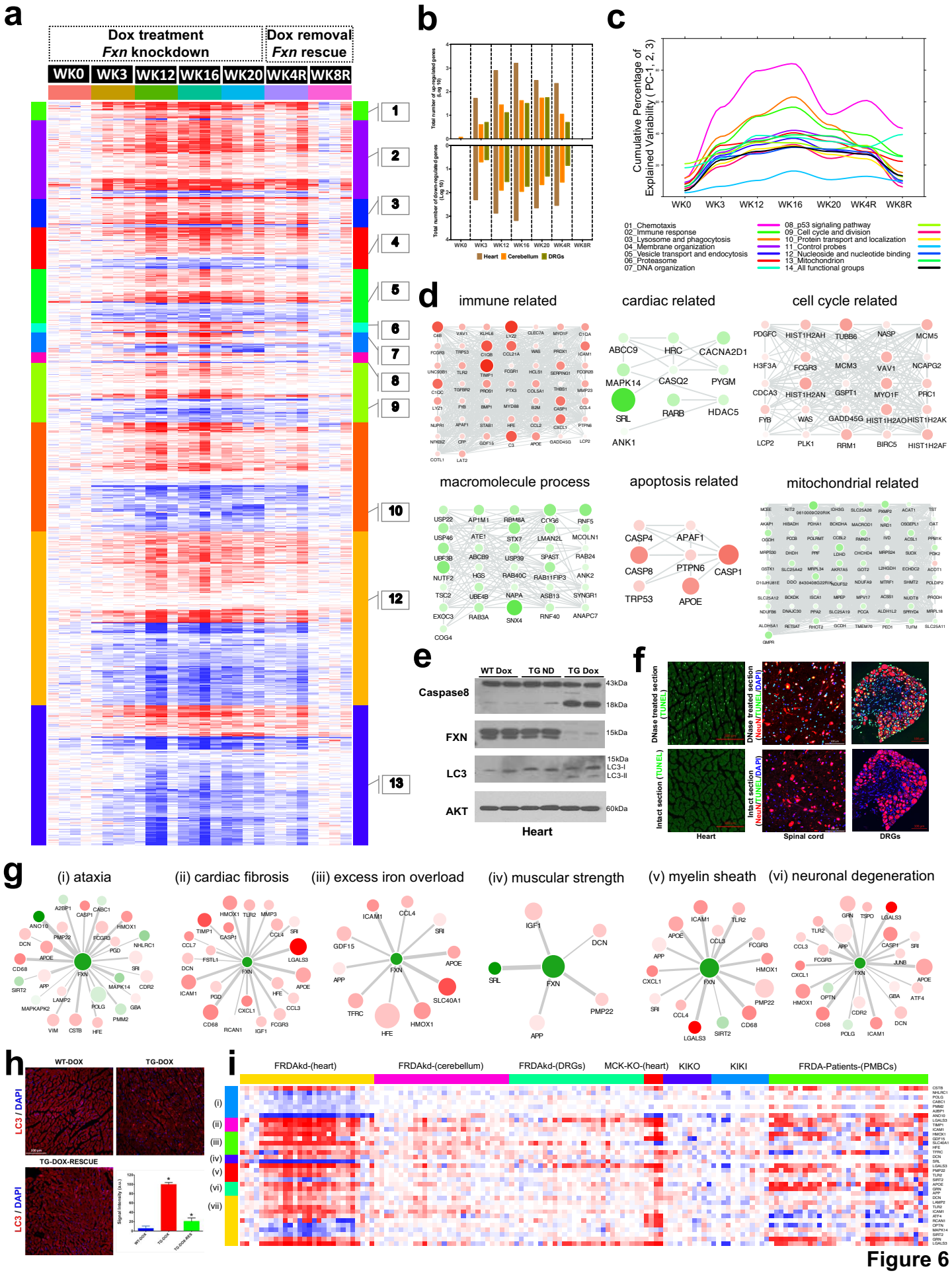
a
Dox treatment
Fxn knockdown
Dox removal
Fxn rescue
WK0
WK3
WK12
WK16
WK20
WK4R
WK8R
1
2
3
4
5
6
7
8
9
10
12
13
b
Total number of up-regulated genes (Log 10)
Total number of down-regulated genes (Log 10)
Heart
Cerebellum
DRGs
c
Cumulative Percentage of Explained Variability (PC-1, 2, 3)
01_Chemotaxis
02_Immune response
03_Lysosome and phagocytosis
04_Membrane organization
05_Vesicle transport and endocytosis
06_Proteasome
07_DNA organization
08_p53 signaling pathway
09_Cell cycle and division
10_Protein transport and localization
11_Control probes
12_Nucleoside and nucleotide binding
13_Mitochondrion
14_All functional groups
d
immune related
cardiac related
cell cycle related
macromolecule process
apoptosis related
mitochondrial related
e
WT Dox
TG ND
TG Dox
Caspase8
43kDa
18kDa
FXN
15kDa
LC3
15kDa
LC3-I
LC3-II
AKT
60kDa
Heart
f
DNase treated section (TUNEL)
DNase treated section (NeuN/TUNEL/DAPI)
Intact section (TUNEL)
Intact section (NeuN/TUNEL/DAPI)
Heart
Spinal cord
DRGs
g
(i) ataxia
(ii) cardiac fibrosis
(iii) excess iron overload
(iv) muscular strength
(v) myelin sheath
(vi) neuronal degeneration
h
WT-DOX
TG-DOX
TG-DOX-RESCUE
LC3 / DAPI
Signal Intensity (a.u.)
i
FRDAkd-(heart)
FRDAkd-(cerebellum)
FRDAkd-(DRGs)
MCK-KO-(heart)
KIKO
KIKI
FRDA-Patients-(PMBCs)
(i)
(ii)
(iii)
(iv)
(v)
(vi)
(vii)

Figure 6

Figure 6: Gene expression analysis of frataxin knockdown mice. (**a**) Heat map of significantly up- and down-regulated genes (rows) in heart tissue of Tg + mice from 0, 3, 12, 16, 20 and plus 4, 8 weeks post dox treatment relative to controls are grouped into 13 functional categories. (**b**) Summary of differentially expressed genes during *Fxn* knockdown and rescue in heart, cerebellum and DRG tissues from four biological replicates. (**c**) Cumulative percent of variability in Tg + gene expression data explained by the first three principal component for each functional category. (**d**) Networks highlighting differentially expressed genes due to *Fxn* knockdown in Tg + mice for selected functional categories. Nodes represents genes and edges are present between nodes when their gene expression correlation is greater than 0.5. Node size and color (red= up-regulation and green= down-regulation) denotes extent of differential expression. (**e**) Western blot analyses of Caspase 8, FXN and LC3 following 20 weeks with or without dox treatment in heart. (**f**) TUNEL assay of heart, spinal cord and DRG neurons at 20 weeks after dox treatment in Tg + mice. (**g**) Literature associated gene networks highlighting differentially expressed genes due to *Fxn* knockdown in Tg + mice for selected key-terms. Nodes represents genes which has pairwise correlation greater than 0.5 with *Fxn* gene and edge size represents strength of their gene expression correlation. Node size correspond to number of PubMed hits with co-occurrence of gene and its corresponding key-term. Node color represents up-regulated (red) and down-regulated (green). (**h**) Representative images and quantification of LC3 staining in heart tissue at 20 weeks after dox treatment. Values represent mean from three biological replicates per group ± SME. One-way ANOVA test *=P≤0.05. (**i**) Heat map depicting expression of key genes (rows) across samples (columns) for seven groups (red corresponds to gene up-regulation and blue to down-regulation). Seven groups represents, (i) ataxia, (ii) cardiac fibrosis, (iii) excess iron overload, (iv) muscular strength, (v) myelin sheath, (vi) neuronal degeneration and (vii) autophagy related genes. Column represents, seven independent datasets obtained from, FRDAsh mice, cardiac specific knockout mice(23), knock-in knockout mice(20), knock-in mice(20) and patient peripheral blood mononuclear cells(44).